Journal of Geophysical Research-Planet, vol 104, pages 24,155-24,176, 1999

Improved general circulation models of the martian atmosphere from the surface to above 80 km

François Forget, Frédéric Hourdin, Richard Fournier,[1] Christophe Hourdin, and Olivier Talagrand

Laboratoire de Météorologie Dynamique du CNRS, Université Paris 6, Paris

Matthew Collins,[2] Stephen R. Lewis and Peter. L. Read

Atmospheric, Oceanic and Planetary Physics, Department of Physics, Oxford University, Oxford, England, United Kingdom

Jean-Paul Huot

European Space Research and Technology Centre, European Space Agency, Noordwijk, Netherlands

Abstract. We describe a set of two "new generation" general circulation models of the Martian atmosphere derived from the models we originally developed in the early 1990s. The two new models share the same physical parameterizations but use two complementary numerical methods to solve the atmospheric dynamic equations. The vertical resolution near the surface has been refined, and the vertical domain has been extended to above 80 km. These changes are accompanied by the inclusion of state-of-the-art parameterizations to better simulate the dynamical and physical processes near the surface (boundary layer scheme, subgrid-scale topography parameterization, etc.) and at high altitude (gravity wave drag). In addition, radiative transfer calculations and the representation of polar processes have been significantly improved. We present some examples of zonal-mean fields from simulations using the model at several seasons. One relatively novel aspect, previously introduced by *Wilson* [1997], is that around northern winter solstice the strong pole to pole diabatic forcing creates a quasi-global, angular-momentum conserving Hadley cell which has no terrestrial equivalent. Within such a cell the Coriolis forces accelerate the winter meridional flow toward the pole and induce a strong warming of the middle polar atmosphere down to 25 km. This winter polar warming had been observed but not properly modeled until recently. In fact, thermal inversions are generally predicted above one, and often both, poles around 60-70 km. However, the Mars middle atmosphere above 40 km is found to be very model-sensitive and thus difficult to simulate accurately in the absence of observations.

1. Introduction

Most of what is currently known about the climate and the general circulation of the atmosphere of Mars still come from the spacecraft missions of the 1970s. Unfortunately, these observational data lacked the temporal and spatial cov-

[1] Now at Laboratoire d'Energie Solaire et Thermique de l'Habitat, Université Paul Sabatier, Toulouse, France.

[2] Now at Hadley Centre for Climate Prediction and Research, United Kingdom Meteorological Office, Bracknell, England.

erage needed to fully characterize the general circulation of the atmosphere, and for several years the details of the general circulation have been derived from numerical simulations performed with general circulation models (GCMs) adapted from the models used for weather forecasting and climate studies for the Earth. On Mars, GCMs have successfully reproduced most of the available observations and have thus been very useful in analyzing and interpreting the data. They have also been used to predict the behavior of the Martian atmosphere and climate in regions where few observational data were available, in particular to predict the behavior of planetary waves and meridional circulations.

A new era of spacecraft exploration of Mars is now beginning. More than ever, general circulation models are needed. On the one hand, these missions will greatly extend the quantity of observations of the Martian climate, and GCMs are the best tools to analyze and interpret these data. For instance, the Thermal Emission Spectrometer (TES) and Pressure Modulated Infrared Radiometer (PMIRR) instruments of the Mars Global Surveyor program are atmospheric sounders which mostly measure atmospheric temperatures, rather than winds or pressure. Interpreting the exact nature of the observed structure will be possible by directly comparing the data with the GCM predictions or by assimilating the data into the models using the powerful data assimilation schemes which have been developed for Earth's meteorology and climatology, as demonstrated for Mars by *Lewis et al.* [1996]. On the other hand, the design of future missions requires a good knowledge of the Martian environment and its variability (for aerobraking, aerocapture, descent and landing, instrument specification, etc.). Because they are able to provide a complete three-dimensional time-dependent atmospheric state, carefully validated GCMs are the best tools available for these aspects of mission design.

For these purposes, very sophisticated models, accounting for all the processes thought to affect the Martian meteorology, are needed. To develop such a model, two groups from the Laboratoire de Météorologie Dynamique (LMD, Paris) and the sub-Department of Atmospheric, Oceanic and Planetary Physics at Oxford University (hereafter AOPP, Oxford) have joined their efforts, with the support of the European Space Agency, Centre National de Recherche Scientifique (CNRS), and the U.K. Particle Physics and Astronomy Research Council. A "new generation" GCM has been developed, based largely on the models previously developed seperately by the two groups, but in which most of the schemes have been improved or redesigned and new parameterizations added. The primary purpose of this paper is to present a detailed description of the resulting model. Some results illustrating the GCM performances have also been included at the end of the paper. More detailed analysis of the Martian climate and further comparisons of the GCM results with the available observations are to be published elsewhere (see, for instance, *Forget et al.* [1998b] ; other papers are in preparation). In particular, this new GCM has been used to produce a Martian climate database, presented in a companion paper [*Lewis et al.*, this issue] along with some comparisons with the available observations.

2. Background

Comprehensive general circulation modeling of the Martian atmosphere began with *Leovy and Mintz* [1969] who successfully adapted the then recently developed terrestrial GCM of the University of California, Los Angeles (UCLA) to Martian conditions. The model predicted atmospheric condensation of CO_2 and the presence of transient baroclinic waves in the winter midlatitudes. Later developments of this model were made at NASA Ames Research Center and have provided a number of insights into our understanding of the Martian climate [see, e.g., *Pollack et al.*, 1981, 1990; *Haberle et al.*, 1993b; *Barnes et al.*, 1993, 1996; *Murphy et al.*, 1995; *Hollingsworth et al.*, 1996].

In 1989 the LMD terrestrial climate model was adapted to Mars by developing a new radiative transfer code [*Hourdin*, 1992a] and a self-consistent parameterization for the condensation and sublimation of CO_2. This model was the first to simulate a full Martian year without any forcing other than insolation [*Hourdin et al.*, 1993, 1995]. It was able to reproduce in a very satisfactory way the seasonal and transient pressure variations observed by the Viking Landers [*Hourdin et al.*, 1995; *Collins et al.*, 1996].

More recently, a similar effort was initiated jointly at the Universities of Reading and Oxford in the United Kingdom. A spectral solver was used in conjunction with a simplified set of physical parameterizations. Original results were obtained on the dynamical regime of baroclinic waves [*Collins and James*, 1995; *Collins et al.*, 1996] and on the boundary-current nature of the low-level cross-equatorial branch of the Hadley Circulation [*Joshi et al.*, 1994].

At about the same time, a new GCM was developed at the Geophysical Fluid Dynamic Laboratory (GFDL) with inclusion of a physical package similar to the Ames model. The model was used to study the role of thermal tides [*Wilson and Hamilton*, 1996], and, separately from *Forget et al.* [1996] (who obtained the same results at LMD at the same time), indicated the importance of extending the vertical coverage of GCM modeling to create a polar warming [*Wilson*, 1997].

In 1995, at the initiative of the European Space Agency, who were seeking an environmental model for mission design on Mars, the LMD and AOPP, Oxford, teamed up to

develop the model presented here and the climate database described in the companion paper by Lewis et al. [this issue].

3. Model Dynamics

The core of an atmospheric general circulation model is the hydrodynamical code dedicated to the temporal and spatial integration of the equations of hydrodynamics. This part, which is based on a rather general formulation of the hydrostatic primitive equations of dynamical meteorology on a sphere, can be adapted directly from terrestrial models. Two distinct formulations have been developed so far: (1) a finite differences or grid point model based on the discretization of the horizontal domain fields on a latitude-longitude grid and (2) a spectral model, in which the horizontal model fields are represented by a truncated series of spherical harmonics.

Each of these formulations offers advantages and disadvantages with regard to accuracy and numerical performance, and both approaches are employed at various centers for climate modeling on Earth. As for Mars, since both formulations had been previously used at LMD (grid point model) and AOPP (spectral model), we chose to keep both kinds as options in order to estimate the likely uncertainty arising from certain types of modeling errors.

The grid point dynamic model is based on the LMD terrestrial model described by *Sadourny and Laval* [1984]. The discretization scheme conserves both potential enstrophy for barotropic nondivergent flows [*Sadourny*, 1975] and total angular momentum for constant surface pressure axisymmetric flow. The latter property was not included in the original terrestrial version but was found to be very important for simulating the Martian atmosphere in order to avoid spurious prograde zonal winds in equatorial regions [*Hourdin*, 1992b]. The model is typically run with a regular resolution of 64×48 grid points horizontally, corresponding to 3.75° latitude by 5.625° longitude. However, in its present version, the grid points can be arbitrarily spread in both latitude and longitude. This offers the possibility of zooming in on a given part of the globe to study the local meteorology, for instance, at a spacecraft landing site. At high latitude a filter is applied near the singularity in the grid at the pole in order to satisfy the Courant-Friedrichs-Lewy numerical stability criterion without going to an excessively small timestep. In the original version of the dynamical code a classical Fourier filter was used, but we found that because the Martian polar atmosphere appears to be much more dynamically unstable than the Earth's polar atmosphere, a more efficient formulation (based on the grouping of adjacent gridpoints together) was necessary to avoid numerical instability.

The AOPP spectral solver was originally developed at the University of Reading [*Hoskins and Simmons*, 1975] and also conserves total angular momentum. A triangular truncation in spectral space at total wavenumber 31, with the nonlinear terms calculated on a 96×48 real space grid, is typically used.

In the vertical, both models use the terrain-following σ coordinate system (σ is pressure divided by surface pressure) in finite difference form. Twenty-five levels are typically used, with the middle of the first three layers located at altitudes of about 4, 19, and 44 m [see *Lewis et al.*, this issue, Table 3]. Compared to the previous versions of the model [see *Hourdin et al.*, 1993, Table 1], the vertical resolution near the surface is substantially enhanced, allowing a much better representation of the atmospheric boundary layer (see section 6.1). Similarly, the middle of the top layer has been extended from 60 km up to about 100 km. This extension not only allows us to explore the meteorological regime at these altitudes, but we found that a deeper model domain allows for the full development of the Hadley circulation and was thus necessary to properly simulate the Martian climate below 50 km. This is discussed further in section 8.

In both the grid point and spectral models, nonlinear interactions between explicitly resolved scales and subgrid-scale processes are parameterized by applying a scale-selective horizontal dissipation operator based on an n time iterated Laplacian Δ^n. For the grid point model, for instance, this can be written $\partial q/\partial t = ([-1]^n/\tau_{\text{diss}})(\delta x)^{2n}\Delta^n q$ where δx is the smallest horizontal distance represented in the model and τ_{diss} is the dissipation timescale for a structure of scale δx. A similar operator is applied to the spectral model fields in spectral space. These operators are necessary to ensure the grid point model numerical stability and to prevent a build up of energy at the truncation limit of the spectral model. In practice, the operator is separately applied to (1) potential temperature, (2) the divergence of the flow, and (3) its vorticity. We respectively use $n = 2$, $n = 1$, and $n = 2$ in the grid point model. In the nominal version of the spectral model, however, $n = 3$ is used for the three fields, following the guidelines given by *MacVean* [1983].

In the upper levels a sponge layer is also used in both models in an attempt to reduce spurious reflections of vertically propagating waves from the model top. Unlike the traditional Rayleigh friction formulation, this operates as a linear drag solely on the eddy components of the vorticity and divergence fields and is not scale-selective. The timescales on which it operates are typically half a day, 1 day, and 2 days at the three uppermost levels, respectively.

4. Radiative Transfer

The radiative transfer through the Martian atmosphere can be affected by the presence of CO_2 gas, mineral dust, water vapor, water ice particles, and CO_2 ice particles. The radiative effects of ozone should generally be negligible [*Lindner*, 1990; *Zurek et al.*, 1992]. This section describes how the effects of gaseous carbon dioxide and suspended dust are included in the model at solar and infrared wavelengths. The radiative effects of water vapor are neglected, since the cold Martian atmosphere cannot sustain more than a few tens of precipitable micrometers of water. In reality, water vapor could slightly increase the gaseous infrared absorption of the lower atmosphere in the northern hemisphere in summer [*Savijärvi*, 1991]. However, the associated error should be small compared to the uncertainties related to the dust radiative properties and spatial distribution. Similarly, the effect of water ice clouds is neglected. Water ice clouds can become optically thick on Mars, but their occurrence is thought to be quite limited in space and time. Nevertheless, new measurements may motivate the development of water cloud parameterizations in the future. The possible radiative effects of CO_2 ice particles during the polar night have been parameterized separately, as explained in section 7.

4.1. CO_2 Gas

4.1.1. Thermal infrared. The treatment of absorption and emission by the strong CO_2 15-μm band is described by *Hourdin* [1992a]. The radiative transfer equation is integrated using the wideband model developed by *Morcrette et al.* [1986]. In its current version the scheme accounts for the Doppler broadening of the molecular lines at low pressure (significant above 50 km) but not for departures from local thermal equilibrium (LTE) (thought to be significant above 70-80 km, near the top of the model). Work is ongoing to include non-LTE effects on cooling in the model. The CO_2 15-μm band, extending from 11.5 to 20 μm, is divided into two widebands representing (1) the central strongly absorbing part (14.2-15.7 μm) and (2) the wings.

4.1.2. Near-infrared absorption. Atmospheric heating due to absorption of solar radiation in the near-IR bands of CO_2 is negligible below 30 km but becomes considerable above 50 km. A simple parameterization has been included which is similar in its effect to heating rates obtained in radiative transfer calculations performed by *Lopez-Puertas and Lopez-Valverde* [1995] which include non-LTE effects. At pressure $p_0 = 700$ Pa and for a mean Mars-Sun distance $r_0 = 1.52$ AU, the heating rate corresponding to a zero solar zenith angle ($\mu = 0$) is taken to be

$$\frac{\partial T}{\partial t}(p_0, r_0, 0) = 1.3 \ \text{K day}^{-1} \quad (1)$$

The heating rate at other pressures p, Mars-Sun distance r, and zenithal angle μ is then computed as follows:

$$\frac{\partial T}{\partial t}(p, r, \mu) = \frac{\partial T}{\partial t}(p_0, r_0, 0) \times \frac{r_0^2}{r^2} \sqrt{\frac{p_0}{p}} \tilde{\mu} (1 + \frac{p_{\text{NLTE}}}{p})^{-1} \quad (2)$$

where p_{NLTE} is a pressure below which non-LTE effects are significant ($p_{\text{NLTE}} = 0.0075$ Pa) and $\tilde{\mu}$ the cosine of the solar zenith angle corrected for atmospheric refraction (we use $\tilde{\mu} = [(1224\mu^2 + 1)/1225)]^{1/2}$). The effect of non-LTE is a strong decrease of the heating above 80 km. In theory, this simple parameterization is not completely consistent since the CO_2 heating is just added to other heating terms without reducing the solar flux available for dust and surface heating below. However, the corresponding maximum reduction of the solar incident flux is always lower than 1.5%, well below the level of other uncertainties related to the dust and the surface properties.

4.2. Dust

4.2.1. Solar radiation. As in the original version [*Hourdin et al.*, 1993, 1995], the radiative transfer equation accounting for the absorption and scattering of solar radiation by the dust is based on the numerical scheme of *Fouquart and Bonel* [1980]. This code was originally developed for the LMD terrestrial GCM and is currently used by the operational model of the European Centre for Medium-Range Weather Forecasts (ECMWF). The upward and downward fluxes are obtained from the reflectances and transmittances of the layers, computed using the Delta-Eddington approximation.

The available studies of Martian dust optical properties have suggested that the single-scattering properties are characterized by an abrupt change around 0.5 μm near the peak of the incident solar flux and that multispectral calculations were essential to obtain accurate results [*Ockert-Bell et al.*, 1997]. Since detailed multispectral calculations would be too expensive in a GCM, we use two broadbands (0.1-0.5 μm and 0.5-5 μm). In order to make use of spectral dust properties, we spectrally average them in each wideband to obtain mean scattering coefficients (extinction coefficient $\tilde{Q}_{\text{ext}}$, single-scattering albedo $\tilde{\omega}$, and asymmetry parameter $\tilde{g}$). The following ponderation laws are used:

$$\tilde{Q}_{\text{ext}} = \frac{\int_{\lambda_1}^{\lambda_2} B_\lambda Q_{ext,\lambda} \, d\lambda}{\int_{\lambda_1}^{\lambda_2} B_\lambda \, d\lambda} \quad (3)$$

$$\tilde{\omega} = \frac{\int_{\lambda_1}^{\lambda_2} B_\lambda Q_{\text{ext},\lambda} \omega_\lambda \, d\lambda}{\int_{\lambda_1}^{\lambda_2} B_\lambda Q_{\text{ext},\lambda} \, d\lambda} \quad (4)$$

$$\tilde{g} = \frac{\int_{\lambda_1}^{\lambda_2} B_\lambda Q_{\mathrm{ext},\lambda} \omega_\lambda g_\lambda \, d\lambda}{\int_{\lambda_1}^{\lambda_2} B_\lambda Q_{\mathrm{ext},\lambda} \omega_\lambda \, d\lambda} \quad (5)$$

where B_λ is the Planck function at 6000 K (representing the solar radiance) and λ_1 and λ_2 are the wavelengths at the boundaries of the band.

Choosing the exact radiative properties to be used by the model remains problematic, however. On the one hand, this is due to the facts that the dust single-scattering properties may vary with altitude, season, and horizontal locations and that the various properties obtained by the different past studies may not be representative. In particular, it is likely that in some conditions, the dust particles can get coated by water ice [*Colburn et al.*, 1989; *Ockert-Bell et al.*, 1997]. On the other hand, the radiative transfer results which are of importance for GCM (e.g., heating rates) are unfortunately extremely sensitive to the dust properties. For instance, the dust single-scattering albedo ω at solar wavelength is thought to be quite high, typically around 0.9. An uncertainty of $\pm 5\%$ then corresponds to an error on the heating rate of about $\pm 50\%$. Dust optical properties have been derived from surface observations (landers) and from orbit. Among the first kind of data, one of the most complete data sets is the spectral single-scattering properties extrapolated over the solar wavelengths by *Ockert-Bell et al.* [1997] from the *Pollack et al.* [1995] Viking Lander data. These data appear to be consistent with the more recent Pathfinder observations [*Markiewicz et al.*, 1999]. However, data obtained from downlooking observation performed in orbit from above the atmosphere seem to give slightly differents results. Wavelength-averaged dust properties were derived by *Clancy and Lee* [1991] on the basis of their analysis of the Viking orbiter infrared thermal mapper (IRTM) emission-phase-function measurements. These observations yielded brighter dust properties, with a higher single scattering albedo and a lower asymmetry parameter (Table 4.2.1). This may result from to the fact that smaller dust particles are sampled from above or that the observation includes the effects of clouds. In practice, Clancy and Lee's dust parameters corresponds to slightly colder temperatures than with the Ockert-Bell dust parameters. Until better data from the upcoming Martian missions are made available, we have been using both kinds of data in the model (Table 4.2.1). However, the results presented in this paper as well as in the companion paper by *Lewis et al.* [this issue] were all obtained using *Clancy and Lee*'s [1991] dust.

4.2.2. Thermal infrared. In the original version of the model, scattering of thermal infrared radiation was not taken into account. This assumption is made in most Earth studies. On Mars, such an assumption is reasonable within the CO_2 15-μm band because of the strong isotropy of the radiation emitted by the gaseous atmosphere (Y. Fouquart, personal communication, 1991). However, we found that at other wavelengths the infrared radiation scattered by the atmospheric dust back to the surface can be nonnegligible (Figure 1), thus changing the surface and atmospheric temperature.

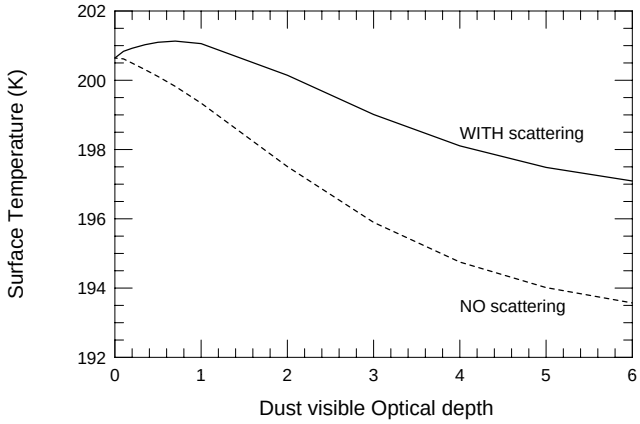

Figure 1. Daily averaged surface temperature computed at Viking Lander 1 site (22°N) at winter solstice ($L_s = 270°$) as a function of dust opacity (results obtained with a one-dimensional radiative-convective version of the general circulation model (GCM) physical package). Scattering of infrared radiation by the airborne dust typically increases the incident IR flux to the surface outside the CO_2 gaseous band by 10-20%. This results in a warming of the surface.

We have therefore included a radiative transfer scheme that accounts for multiple scattering by dust particles outside the CO_2 15-μm band. It is based on the two-stream hemispheric mean source function code described by *Toon et al.* [1989]. The infrared spectrum outside the CO_2 15-μm band is divided into two widebands, one for the 9-μm silicate band (5-11.5 μm) and one for the rest of the infrared spectrum (20-200 μm). Until more accurate data are made available, we use a set of synthetic single scattering spectral properties of the Martian dust specifically formulated for this GCM and described by *Forget* [1998]. This model was developed by modifying the long-standing *Toon et al.* [1977] dust model (based on the optical properties of a clay sample called Montmorillonite 219b) in order to accurately match the Mariner 9 observations of the 1971 global dust storm at every IR wavelength, without restriction to any particular hypothesis for the actual dust composition. In each wideband, wavelength-integrated mean dust single-scattering properties were computed using (3), (4) and (5), with B_λ being the blackbody intensity at 215 K, a typical mean temperature on Mars (Table 4.2.1). This discretiza-

Table 1. Averaged Atmospheric Dust Single Scattering Parameters Used in the Solar and Thermal Infrared Radiative Transfer Code in the Current Version of the Model with the Infrared to Visible Opacity Ratio $\tau_{9\mu m}/\tau_{0.67\mu m}$ set to 2.

	Band, μm	$\tilde{Q}_{ext}/Q_{ext}(0.67\mu m)$	$\tilde{\omega}$	$\tilde{g}$
Solar radiation (1)[a]	0.1-0.5 μm	0.878	0.665	0.819
	0.5-5 μm	1.024	0.927	0.648
Solar radiation (2)[b]	0.1-0.5 μm	1.0	0.920	0.55
	0.5-5 μm	1.0	0.920	0.55
Thermal radiation[c]	5-11.6 μm	0.253	0.470	0.528
	11.6-20 μm	0.405	0.541	0.551
	20-200 μm	0.166	0.370	0.362

Results presented in this paper were obtained using solar radiation properties (2).

[a]Computed from *Ockert-Bell et al.* [1997].

[b]Computed from *Clancy and Lee* [1991].

[c]Computed from *Forget* [1998].

tion in two widebands was found to introduce less than 10% error compared to a more sophisticated narrowband computation. In the 15-μm band, absorption by the dust is added to the absorption by CO_2, using a mean absorption parameter $\tilde{Q}_{abs} = (1-\tilde{\omega})\tilde{Q}_{ext}$, with $\tilde{\omega}$ and $\tilde{Q}_{ext}$ computed as above.

The scaling of dust opacity in the infrared compared to the visible is also a key parameter of the dust model since it controls the local radiative balance of the atmosphere and the surface. This ratio is highly sensitive to the actual dust size distribution, which is poorly known since each spectral region is sensitive to different particle sizes [see *Zurek* 1982; *Forget*, 1998]. In the original model a ratio of about 1.2 had been used, following *Pollack et al.* [1979] as in most other existing Mars GCMs then [e.g., *Pollack et al.*, 1990; *Wilson and Hamilton*, 1996]. However, measurements of the dust optical depth made separately at solar and infrared wavelengths at the same time and location suggest a visible (0.67 μm) to infrared (9 μm) ratio of about 2-2.5 [*Martin*, 1986; *Clancy et al.*, 1995]. In the baseline version of the model we therefore scale the dust opacities τ from the ratio $\tau_{9\mu m}/\tau_{0.67\mu m} = 2$ (Table 4.2.1).

4.2.3. Dust spatial distribution. In the baseline version of the model, the dust mixing ratio is prescribed and the dust is not transported by winds (other versions of the model include this capability [*Forget et al.* 1998a]). The dust mixing ratio is taken to be constant in the lower atmosphere up to a level above which it rapidly declines, consistent with the available spacecraft observations. Following *Pollack et al.* [1990], most GCMs (including the previous version of this model) have used the dust vertical distribution derived by *Conrath* [1975] from considerations of particle sedimentation and eddy mixing. The dust mass mixing ratio q was defined as a function of pressure p; that is,

$$q = q_0 \exp[\nu(1 - p_0/p)] \qquad p \le p_0$$
$$q = q_0 \qquad p > p_0 \qquad (6)$$

where q_0 is a constant determined by the prescribed optical depth at the reference pressure level $p_0 = 700$ Pa and ν is a constant that determines the shape of the function. *Conrath* [1975] estimated $\nu = 0.007$ during dust storms, but *Pollack et al.* [1990] (and following most other GCMs) used $\nu = 0.03$, thought to represent more typical conditions. In reality, observations at the limb by the camera aboard Mariner 9 [*Anderson and Leovy*, 1978] and Viking [*Jaquin et al.*, 1986] have shown that the dust vertical distribution strongly varies with space and time, with dust confined near the surface in the polar regions or reaching very high altitudes in the tropics during dust storms. Representing these variations with (6) by varying ν would have led to an unrealistic vertical distribution. We therefore used a modified version of (6):

$$q = q_0 \exp\left\{0.007\left[1 - (p_0/p)^{(70\text{ km}/z_{max})}\right]\right\} \qquad p \le p_0 \quad (7)$$

where z_{max} is the altitude (km) of the top of the dust layer. Equation (7) matches (6) under the conditions for which the later was originally designed by Conrath ($\nu = 0.007$, $z_{max} = 70$ km) but remains realistic for thinner dust layers [see *Lewis et al.*, this issue, Figure 3]. The climatological altitude of the top of the dust layers can be deduced from the analysis by *Anderson and Leovy* [1978] and *Jaquin et al.* [1986]. To first order, these measurements can be summarized and represented by the function $z_{max} = 60 + 18\sin(L_s - 160°) - 22(\sin\phi)^2$, with L_s beeing the solar longitude and ϕ being latitude. This equation is

currently used in most of our simulations. However, we usually keep the reference mixing ratio q_0 constant horizontally over the planet. Indeed, although slight spatial variations of the dust optical depth have been measured by *Martin* [1986] and *Martin and Richardson* [1993], no simple dependence on latitude or longitude can be determined.

5. Surface Processes

Surface temperature evolution is governed by the balance between incoming fluxes (direct solar insolation, thermal radiation from the atmosphere and the surface itself, and turbulent fluxes) and thermal conduction in the soil. The parameterization of this last process is based on the sophisticated 11-layer soil model originally developed for the LMD Martian GCM (described by *Hourdin et al.* [1993]). A vertically homogeneous soil is assumed, and the spatially varying soil and surface properties, that is, thermal inertia and albedo, are currently based on the Viking IRTM observations analyzed by *Palluconi and Kieffer* [1981] (thermal inertia) and *Pleskot and Miner* [1982] (albedo) extended to the polar regions using the recent results from *Paige et al.* [1994] and *Paige and Keegan* [1994]. It has been suggested that the thermal inertia deduced by *Palluconi and Kieffer* [1981] may be overestimated due to weaknesses in the retrieval model [*Haberle and Jakosky*, 1991] but it is retained for the present in the absence of more reliable information. More accurate data from the upcoming missions will be adopted as soon as available. A third map is used by the model for the surface orography. The accurate measurements from the Mars Orbiter Laser Altimeter (MOLA) aboard Mars Global Surveyor will be used as soon as possible. This paper was written before these data were made available. Three data sets were then available for modelers : the Mars Consortium [*Wu*, 1978], the U.S. Geophysical Survey digital elevation model (often called DTM ; see *Davies* [1992]), and the eigth-degree and order spherical harmonic model derived from radio occultation data by *Smith and Zuber* [1996]. The choice between these data sets remained controversial. The simulated zonal-mean fields presented in this paper were obtained using the DTM data set, which accounts for fine structures not represented in *Smith and Zuber*'s [1996] smooth topography and which provides some information in the southern polar region, where the Mars Consortium map suffered from a lack of data. In fact, such zonal-mean fields are not very sensitive to the details of the topography, and almost similar figures would have been obtained with the other data sets.

6. Subgrid-Scale Dynamics

6.1. Turbulent Diffusion in the Planetary Boundary Layer

Accurate description of near-surface conditions is an increasing requirement for Martian GCMs in order to predict accurate surface drags, dust lifting, tracer transport, and near-surface conditions for mission design. In turn, Mars is a challenging planet for parameterization of boundary layer dynamics, the very shallow (about 100 m) and strongly stratified nocturnal boundary layer evolving during the day in a very deep and fully convective layer of several kilometers.

As in most GCMs, boundary layer dynamics is accounted for by a turbulent closure scheme based on the concept of turbulent viscosity plus a convective adjustement in case of unstable temperature profiles. The turbulent mixing of any state variable a (horizontal wind components or potential temperature) is computed as

$$\frac{\partial a}{\partial t} = \frac{1}{\rho}\frac{\partial}{\partial z} K \rho \frac{\partial a}{\partial z} \tag{8}$$

where K takes different values K_u and K_θ for (u, v) and θ, respectively. In the bottom layer the turbulent surface flux is given by $\rho C_d U_1 (a_1 - a_0)$, where a_1 and a_0 are the variable values in the first atmospheric layer and at the surface ($a_0 = 0$ for winds), U_1 is the wind velocity in the first layer, and C_d is the drag coefficient. Because of the small depth of the first layer ($z_1 \sim 4$ m), we can assume that the wind profile in the first meters above the surface is logarithmic and simply use

$$C_d = \left(\frac{\kappa}{\ln \frac{z}{z_0}} \right)^2 \tag{9}$$

where κ is the von Karman constant ($\kappa = 0.4$) and z_0 is the roughness coefficient. We assume that $z_0 = 0.01$ m everywhere on Mars, as suggested by *Sutton et al.* [1978] for the Viking Lander sites.

The scheme has been recently improved by introducing a new parameterization for K_u and K_θ based on Mellor and Yamada's [1982] unstationary 2.5-level scheme. With respect to the original Mellor and Yamada scheme, we use a modified set of stability functions derived by *Galperin et al.* [1988] to solve some numerical instability problems in the scheme, and the computation of the turbulent mixing length is replaced by *Blackadar*'s [1962] law, $l(z) = \kappa z/(1 + \kappa z/l_0)$, where l_0 is a reference length scale that we fixed to a value of 160 m.

Computation of mixing coefficients is based on an equation for the evolution of the turbulent kinetic energy(TKE) E:

$$\frac{\partial E}{\partial t} = \frac{q^3}{l}\left(S_u G_u + S_\theta G_\theta - \frac{1}{b_1} \right) + \frac{\partial}{\partial z} K_E \frac{\partial E}{\partial z} \tag{10}$$

with

$$q = \sqrt{2E} \tag{11}$$

$$M = \sqrt{\left(\frac{\partial u}{\partial z}\right)^2 + \left(\frac{\partial v}{\partial z}\right)^2} \tag{12}$$

$$G_u = \frac{l^2}{q^2} M^2 \tag{13}$$

$$G_\theta = -\frac{l^2}{q^2}\frac{g}{\theta_0}\frac{\partial \theta}{\partial z} \tag{14}$$

$$S_u = \frac{\alpha_1 + \alpha_2 G_\theta}{(1+\alpha_3 G_\theta)(1+\alpha_4 G_\theta)} \tag{15}$$

$$S_\theta = \frac{\alpha_5}{1+\alpha_3 G_\theta} \tag{16}$$

$$S_E = \alpha_6 \tag{17}$$

The coefficients α_n and b_1 take the constant values (α_1, α_2, α_3, α_4, α_5, α_6, b_1) =(0.393, -3.09, -34.7, -6.13, 0.494, 0.38, 16.6). Here θ_0 is the mean potential temperature. Within this context, the corresponding turbulent diffusion coefficients are $K_u = qlS_u$ for velocity, $K_\theta = qlS_\theta$ for potential temperature, and $K_E = qlS_E$ for TKE.

Figures 2a and 2c show results from one-dimensional (1-D) simulation obtained with this model with the same vertical discretization as for 3-D GCM simulations. The vertical wind and temperature structures are similar to those obtained by *Haberle et al.* [1993a] with a strong decrease of the planetary boundary layer height at night and an associated nocturnal jet with wind magnitudes 20% above the large-scale geostrophic wind.

In the reference parameterization presented above, we use an implicit time scheme except for K. However, even with this classical implementation, the model requires very small time steps (here about 1000 times longer than in the GCM), especially at night. The instability in those strongly stratified conditions was attributed to the strong coupling between wind shear and TKE: for large time steps, the TKE evolution cannot be estimated without taking into account the wind shear reaction during the time step. We therefore derived a simplified but much more robust parameterization in which an estimation of the wind shear evolution under the effect of TKE is introduced in the computation of TKE. This evolution is given by

$$\left(\frac{\partial M}{\partial t}\right)_{z,t} = \frac{\partial^2}{\partial z^2}\left(K_{u,z,t} M_{z,t}\right) \tag{18}$$

For fixed values of fluxes $K_u M$ at the two neighboring levels, (18) gives a simple estimation of the local coupling between TKE and wind shear. In the stable limit ($q \longrightarrow 0$) and neglecting turbulent diffusion of E, the system of equations (10)-(17) reduces to

$$\frac{\partial E}{\partial t} = \frac{q^3}{l}\left(\frac{-\alpha_2}{\alpha_3\alpha_4 \frac{g}{\theta_0}\frac{\partial \theta}{\partial z}} M^2 + \frac{\alpha_5}{\alpha_3} - \frac{1}{b_1}\right) \tag{19}$$

and the resulting coupled system of (18) and (19) can be solved analytically in the stationary case ($\partial/\partial t = 0$ in equations).

In practice, for a large time step Δt suitable for the GCM, the TKE is updated in two steps:

$$M^2_{z,t+\Delta t} \approx \frac{M^2_{z,t}}{S_{u,z,t} G_{u,z,t}}\left(\frac{1}{b_1} - S_{\theta,z,t} G_{\theta,z,t}\right) \tag{20}$$

and

$$E^{3/2}_{z,t+\Delta t} \approx \frac{E_{z,t}}{\sqrt{2} l(z) M_{z,t+\Delta t}} \left(\frac{(z^+ - z) K_{u,z^-,t} M_{z^-,t} + (z - z^-) K_{u,z^+,t} M_{z^+,t}}{z^+ - z^-}\right) \tag{21}$$

where z^- and z^+ are the altitudes of the layer below and above, respectively.

Stationarity means that the time constants for turbulence are shorter than the time step, which is approximately true here. However, the stable approximation is not valid for daytime conditions, but, then, the mixing is essentially done by convection. Under such conditions the *Mellor and Yamada* [1982] parameterization is probably not valid anyway. The derivation of the scheme and analysis will be detailed in a forthcoming dedicated paper. Nevertheless, we show here some comparisons of the GCM parameterization with the full parameterization presented previously. Figures 2b and 2d show 1-D simulation results using this approximate procedure with the standard GCM time step (48 steps per day). Convergence with the reference simulation (Figures 2a and2c) is satisfactory with the exception of the strong day-night transition during which all state variables undergo variations which are faster than the GCM time step and so cannot be fully reproduced by the approximate parameterization. This convergence is the main argument for the validity of the simpified GCM scheme.

In Figure 3 in situ high-frequency measurements obtained by the Viking Lander 1 in spring are compared with 1-D model results. These measurements were made at 1.6 m above the surface, whereas the center of the first GCM layer is around 4 m. This altitude difference does not allow an exact comparison, especially for the wind at night, when stratification is very strong immediately above the surface. Another major source of differences between model and observations is the convective adjustment, which is not

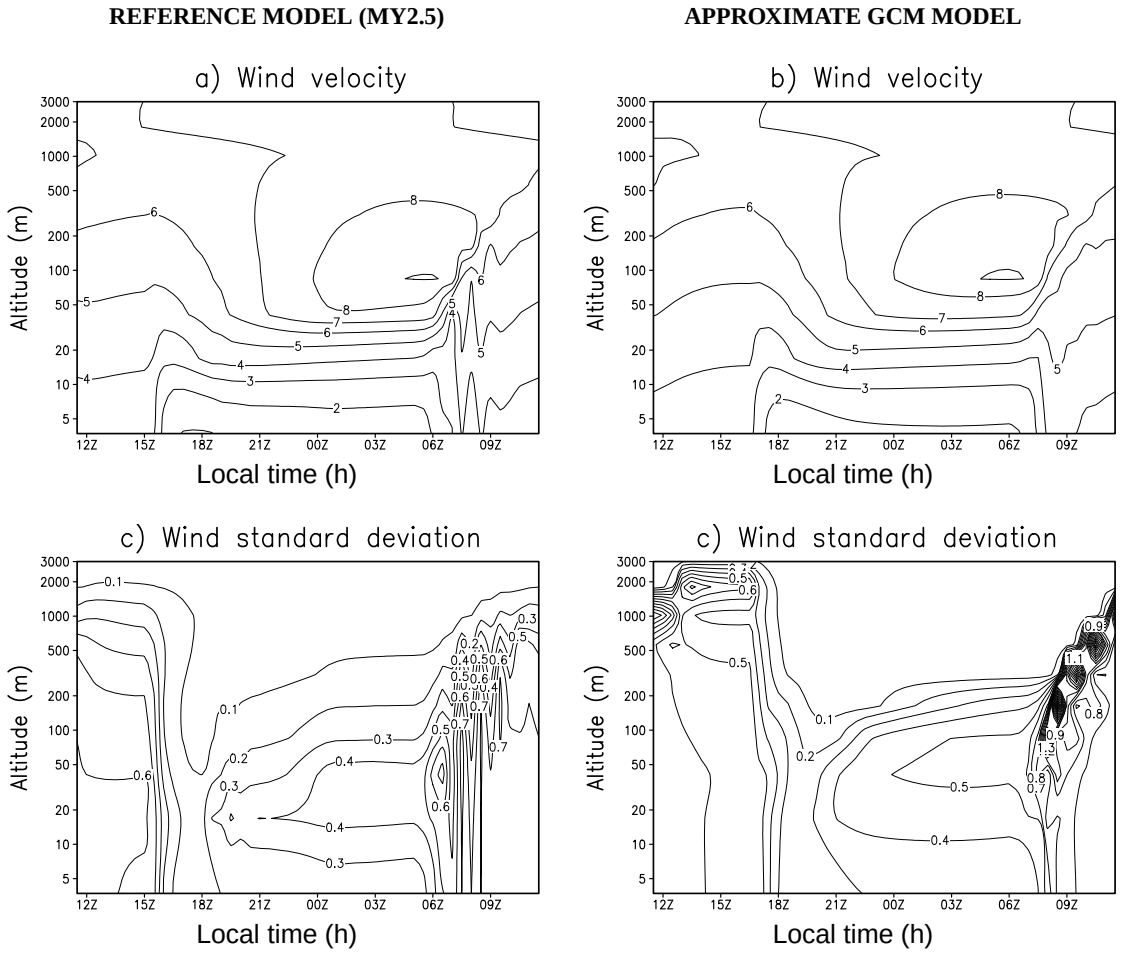

Figure 2. (Figures 2a and 2b) Horizontal wind mean velocity (m s^{-1}) and (Figures 2c and 2d) standard deviation of wind strength q due to turbulence (m s^{-1}) simulated by the reference *Mellor and Yamada* [1982] 2.5 model (left) and the proposed parameterization (right) useable with the GCM's 30 minute timestep. Results in both cases were obtained with a 1-D version of the GCM physical package for conditions at the Viking Lander 1 site (22°N) in spring ($L_s = 45°$). The model is forced thermally by radiation (visible dust opacity: 0.5; surface albedo: 0.32; surface thermal inertia: 290 J m^{-2} $s^{-1/2}$ K^{-1}) and dynamically by a geostrophic wind of 7 m s^{-1}.

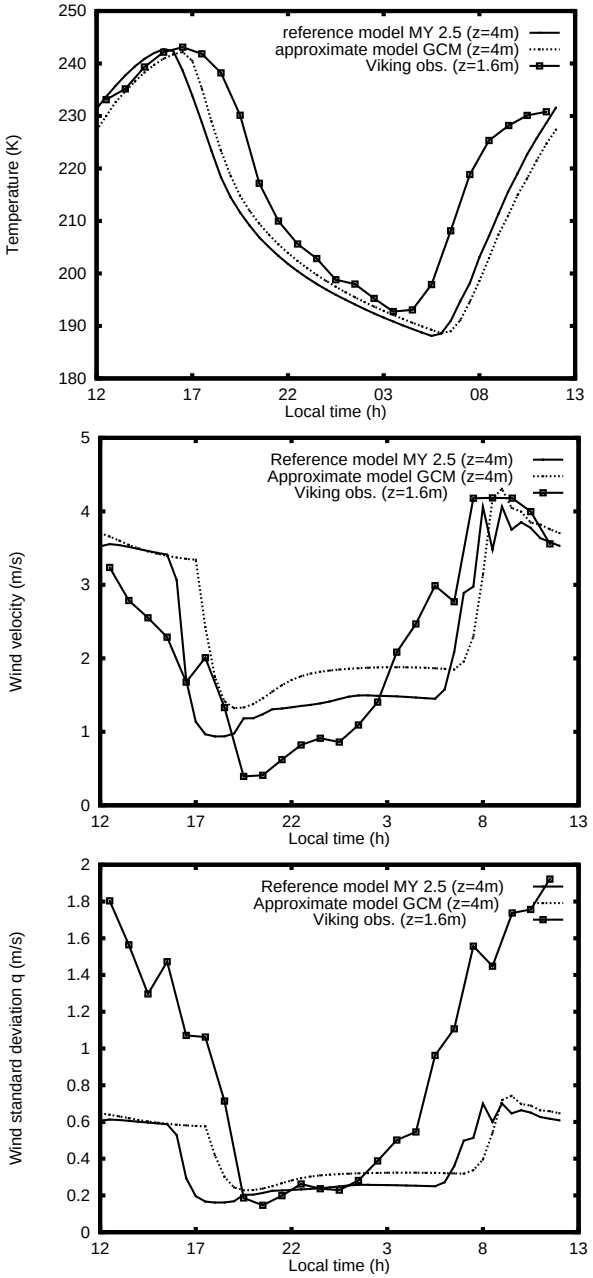

Figure 3. A comparison of Viking Lander 1 observations of temperature, wind mean velocity and standard deviation q measured 1.6 m above the surface during sol 554 ($L_s = 45°$) with results from the 1-D boundary layer scheme at about 4 m. The model parameters are the same as in Figure 2. The high frequency Viking data were kindly provided by J.E. Tillman, Viking Computer Facility (1993).

associated with any TKE increase in the present model. This explains the low TKE values simulated during the day, whereas Viking actually recorded wind fluctuations as high as 2 m s^{-1}. This difference does not alter the mean wind predictions significantly, however. The mean wind velocities predicted by the combined boundary layer-convection schemes seem to match closely the observations. More comparisons concerning the simulation of variations in wind direction with the full 3-D GCM are given by *Lewis et al.* [this issue]. Altogether, it can be concluded that the proposed turbulence model allows economical and realistic estimations of most surface environmental variables and their diurnal evolution.

6.2. Convection

As in the original LMD model, we use a standard energy-conserving convective adjustment scheme which rapidly mixes heat and momentum in convectively unstable layers. To account for the fact that, in reality, the mixing of momentum depends upon the actual mass fluxes involved in the convection, the intensity of the momentum mixing is a function of the intensity of the initial vertical instability [*Hourdin et al.*, 1993].

6.3. Representation of the Subgrid-Scale Orography and Gravity Waves

The orography used in the GCM is smoothed to the horizontal resolution of the model. Direct effects of variations of the orography on scales smaller than the grid scale on the large-scale flow are effectively ignored. These subgrid-scale variations can, however, have a significant impact on the resolved circulation of the atmosphere, so their effects should be parameterized in some way. More specifically, the subgrid-scale mountains can influence the large-scale (explicitely resolved) flow in two ways: (1) by producing a form drag on the flow at low levels and (2) by exciting internal gravity waves which can propagate in the vertical, break, and decelerate the flow far away from the mountains themselves. We have chosen to parameterize these two effects using, for (1), the low-level drag scheme of *Lott and Miller* [1997] and for (2) the gravity wave drag scheme of *Miller et al.* [1989] and *Baines and Palmer* [1990], which was itself developed from the original scheme of *Palmer et al.* [1986]. Both of these schemes are in current operational use at the European Centre for Medium-Range Weather Forecasting. Full details of the implementation and validation of the low-level drag and gravity wave drag parameterization schemes are given by *Collins et al.* [1997]. The impact of the scheme on the performance of the model is illustrated in section 8.3 of the present paper.

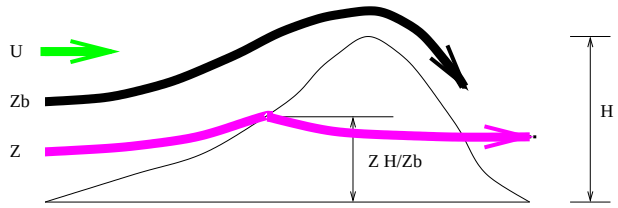

Figure 4. Schematic representation of the low-level flow behavior in the subgrid scale orographic drag parameterization scheme. Adapted from *Lott and Miller* [1997].

6.3.1. Low-level drag parameterization. We define the nondimensional height of a single mountain, H_N, as

$$H_N = \frac{NH}{|U|} \tag{22}$$

where H is the maximum height of the mountain, U is the speed of the wind incident on the mountain, and N is the Brunt-Väisälä frequency.

At small values of H_N all the air flows over the mountain and gravity waves are freely generated (see section 6.3.2). There is no low-level form drag in this case. At large values of H_N, part of the low-level air flow goes around the mountain, producing a significant drag on the low level flow. Figure 4 shows a schematic of the flow at large H_N.

The drag D on the low-level flow can be written as

$$D(z) = -\rho\, C_d\, l(z)\, \frac{u|u|}{2} \tag{23}$$

where ρ is the density, C_d is a drag coefficient of order unity, and $l(z)$ is a length scale based on the horizontal scale of the intersection of the mountain with the incident flow. For an elliptical mountain, that is,

$$h = \frac{H}{1 + \dfrac{x^2}{a^2} + \dfrac{y^2}{b^2}} \qquad b > a \tag{24}$$

then

$$l(z) = 2b\sqrt{\frac{Z_b - z}{z}} \tag{25}$$

where Z_b is the upstream elevation of the lowest isentrope that goes over the mountain. Z_b can be written as

$$Z_b = H\frac{(H_N - H_{NC})}{H_N} \tag{26}$$

where H_{NC} is a critical nondimensional mountain height of order unity.

In a GCM grid box, there is often more than one mountain, and we must take account of this. At a given altitude z the intersection between the mountains and the model layer approximates to an ellipsoid of eccentricity

$$(a', b') = (a, b)\sqrt{\frac{Z_b - z}{z + \mu}} \tag{27}$$

where μ is the standard deviation of the subgrid-scale orography (Figure 5). Then $l(z)$ can be written approximately as

$$l(z) = 2\max(b\cos\psi, a\sin\psi)\sqrt{\frac{Z_b - z}{z + \mu}} \tag{28}$$

where ψ is the angle between the incident flow and the normal ridge direction θ (Figure 5). We note that if L is the width of the grid box, then for $\psi = 0$ there are $L/2a$ ridges in the box and for $\psi = \pi/2$ there are $L/2b$ ridges in the box. Hence

$$l(z) = \frac{L^2}{2}\sqrt{\frac{Z_b - z}{z + \mu}}\max\left(\frac{\cos\psi}{a}, \frac{\sin\psi}{b}\right) \tag{29}$$

If σ is the anisotropy of the orography and γ is the slope (Figure 5), we note that $a \approx \mu/\sigma$ and $a/b \approx \gamma$. Hence the model low-level drag is

$$\begin{aligned} D(z) &= -C_d \max(2 - \frac{1}{r}, 0)\rho\frac{\sigma}{2\mu}\sqrt{\frac{Z_b - z}{z + \mu}} \\ &\quad \times \max\left(\frac{\cos\psi}{a}, \frac{\sin\psi}{b}\right)\frac{U|U|}{2} \end{aligned} \tag{30}$$

where

$$r = \frac{\cos^2\psi + \gamma\sin^2\psi}{\gamma\cos^2\psi + \sin^2\psi} \tag{31}$$

For convenience, and for consistency with the gravity wave drag scheme described below, we substitute the function $B\cos^2\psi + C\sin^2\psi$, ($B$ and C are defined in section 6.3.2) for the expression $\max\left(\dfrac{\cos\psi}{a}, \dfrac{\sin\psi}{b}\right)$. In the GCM the term $D(z)$ is evaluated quasi-implicitly to ensure numerical stability.

6.3.2. Gravity wave drag. Full details of the scheme are given by *Lott and Miller* [1997], *Miller et al.* [1989], *Baines and Palmer* [1990] and *Palmer et al.* [1986] but the essentials are briefly reproduced here for completeness.

It is common in parameterizing gravity wave drag to assume a single gravity wave, with some characteristic wavelength, that propagates from the surface of the model only in the vertical plane. Schemes that represent ensembles of gravity waves are computationally very expensive and, as yet, are little tested even in terrestrial climate models. The

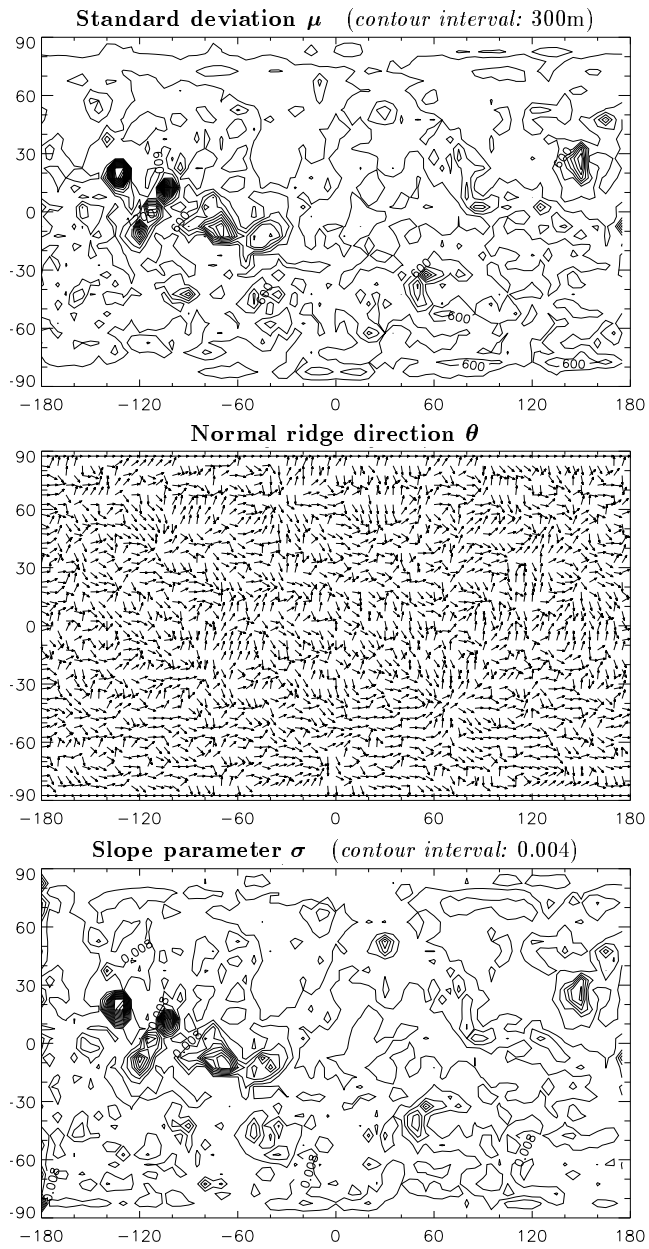

Figure 5. Subgrid-scale orography parameters used by the low-level drag and gravity wave drag parameterization (see text). These have been calculated from the Mars Digital Topographic Map (DTM) [*Davies*, 1992] at $1^\circ \times 1^\circ$ resolution with $h(x,y)$ representing the orography within the grid box defined at N points and $\bar{h}$ representing the mean orography; $\mu = \frac{1}{N}\sqrt{\sum(h-\bar{h})^2}$, and $\theta = \frac{1}{2}\arctan(L/M)$, where $M = \overline{\partial h/\partial x\ \partial h/\partial y}$ and $L = \frac{1}{2}\left((\partial h/\partial x)^2 - (\partial h/\partial y)^2\right)$. The slope parameter σ is defined by $\sigma^2 = \overline{(\partial h/\partial x')^2}$, where $x' = x\cos\theta + y\sin\theta$ and $y' = y\cos\theta - x\sin\theta$. A fourth parameter (not shown) is the anisotropy (shown by *Collins et al.* [1997]): $\gamma = \sqrt{(\partial h/\partial y')^2/(\partial h/\partial x')^2}$.

vector surface stress induced by a single gravity wave generated by a single elliptical mountain, of the form given by (24), can be written as [*Phillips*, 1984]

$$\tau = \rho U N H^2 b G(B\cos^2\psi + C\sin^2\psi, (B-C)\sin\psi\cos\psi) \quad (32)$$

where $B = 1 - 0.18\gamma - 0.04\gamma^2$, $C = 0.48\gamma + 0.3\gamma^2$, G is a constant of order unity, and all the other symbols are as defined in section 6.3.1. Summing over all mountains in the grid box, the model gravity wave stress becomes

$$\tau = \rho U N \mu\sigma G(B\cos^2\psi + C\sin^2\psi, (B-C)\sin\psi\cos\psi). \quad (33)$$

We now consider what happens when the gravity wave propagates vertically. We assume that the stress at any level is parallel to the surface stress and can be written

$$\tau = |\tau| = \kappa\,\rho\,U\,N\,\delta h^2 \quad (34)$$

where $\kappa = \mu\sigma G|(B\cos^2\psi + C\sin^2\psi, (B-C)\sin\psi\cos\psi)|$ and δh can be thought of as the vertical isentropic displacement induced by the propagating gravity wave. We then judge the effect of the wave on the mean flow by calculating the minimum Richardson number attainable, that is, the Richardson number that is "felt by the gravity wave":

$$Ri_{\min} = Ri\frac{1 - \dfrac{N\,\delta h}{U}}{\left(1 + Ri^{1/2}\,\dfrac{N\,\delta h}{U}\right)^2}. \quad (35)$$

Following *Lindzen* [1981] the saturation hypothesis is employed. When $Ri_{\min}$ is greater than some critical value Ri_c, the stress remains constant with height, the gravity wave continues to propagate vertically, and $Ri_{\min}$ is evaluated at the next model level. This is repeated until $Ri_{\min}$ drops below the critical value Ri_c and the wave is deemed to have broken. Then a new value for the isentropic displacement, δh, and hence a new value for the stress, is calculated in order to keep $Ri_{\min} = Ri_c$. The whole process is repeated until the top of the model is reached and the stress is assumed to be zero, that is, the waves are assumed to be dissipated somewhere in the atmosphere. The tendencies are calculated from the vertical derivative of the stress profile.

The scheme represents stationary wave critical level absorption since, when the component of the wind in the direction of the surface stress approaches zero, the Richardson number becomes very large, causing the wave amplitude to become very small. The wave is thus absorbed at the critical level, and the stress is set to zero above the critical line.

7. CO_2 Condensation and Sublimation

The treatment of this uniquely Martian process has been significantly improved in the new version of the model. A

detailed description and a numerical expression of the new scheme are given by *Forget et al.* [1998b]. CO_2 condenses when the local temperature is predicted to fall below the condensation temperature, releasing the latent heat required to keep the solid-gas interface at the condensation temperature. Conversely, when CO_2 ice is heated, it partially sublimes to keep its temperature at the frost point temperature. The model now allows for the possible sublimation of sedimenting CO_2 ice particles in warmer atmospheric layers as they descend to the ground. Minor components of the energy budget are included (e.g., the release of potential energy by CO_2 ice particles during their fall and the heat consumption to warm the particles as the CO_2 frost temperature increases with the local pressure). These components were found to be far from negligible in practice. Also, a correction is now included to account for the mass, heat, and momentum redistribution between the model layers and between the layers and the surface due to condensation or sublimation in $\sigma = p/p_0$ coordinates. Last, the boundary layer scheme has been modified so that the turbulent atmospheric mixing takes into account the fact that the atmosphere can never be colder than the CO_2 frost point.

In the original model, as in every GCM so far, the condensed CO_2 was assumed to precipitate instantaneously to the surface without changing the properties of the atmosphere and the cap. The available observations of the condensing polar caps suggest that reality may be more complex. The Mariner 9 infrared interferometer spectrometer (IRIS) and Viking IRTM instruments measured a significant reduction of the infrared flux emitted by the condensing cap in the polar night [*Kieffer et al.*, 1976]. This reduction has been attributed to the radiative effect of CO_2 snowfalls (falling snow particles or fresh snow deposits). [*Forget et al.*, 1995]. By affecting the radiative balance of the polar regions, these CO_2 snowfalls and deposits are thought to significantly decrease the amount of CO_2 condensing in the polar caps and thus affect the global climate [*Forget and Pollack*, 1996].

To account for this process, we mimic the radiative effect of the CO_2 clouds and fresh snow by decreasing the surface emissivity ε when atmospheric condensation is predicted by the model. The details of the scheme are given by *Forget et al.* [1998b]. In summary, we based our calculations on simple physical considerations (radiative transfer through the CO_2 ice particles, evolution of the snow properties on the ground). The following governing equation was adopted:

$$\frac{\partial \varepsilon}{\partial t} = -1.5 \times 10^{-4} \, \frac{\varepsilon^4}{r} \, \frac{\partial m}{\partial t} + \frac{1}{\mathcal{T}}(1 - \varepsilon) \qquad (36)$$

where $\partial m / \partial t$ is the total atmospheric condensation rate

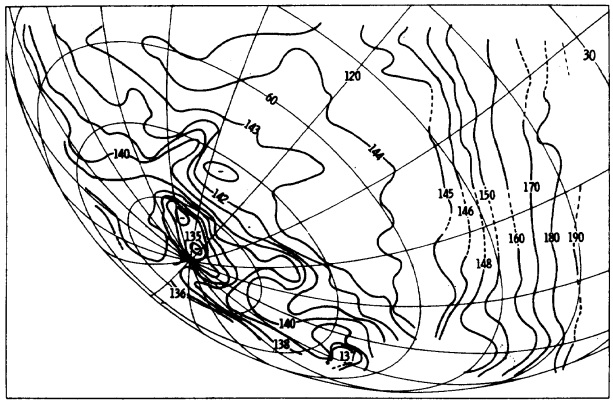

(a) Brightness temperatures observed by Viking (K)

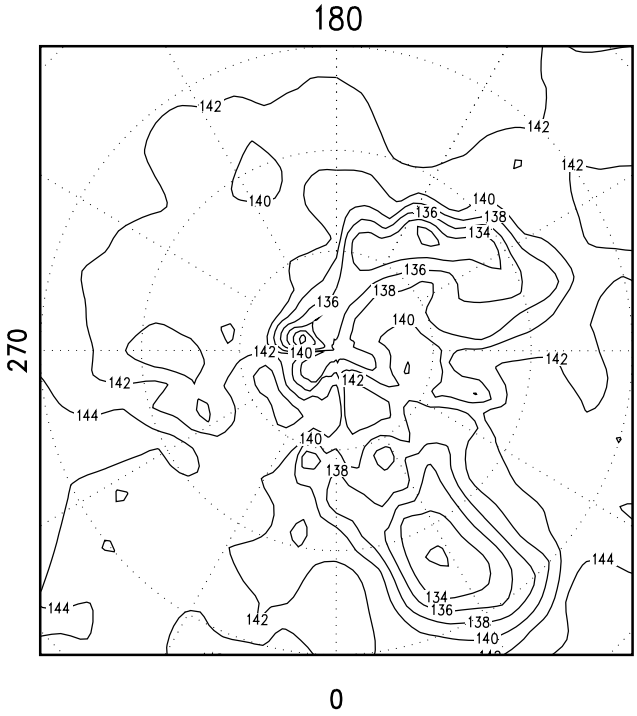

(b) Brightness temperatures simulated by the model (K)

Figure 6. Examples of spatial patterns of the 20-μm brightness temperatures (a) observed by the Viking infrared thermal mapper (IRTM) in the winter south polar region at $L_s = 93°$ (Reprinted with permission from *Kieffer et al.* [1976], Copyright 1976, American Association for the Advancement of Science) and (b) simulated by the model with the parameterization of the CO_2 snowfalls which are thought to locally decrease the outgoing infrared flux, thus creating low brightness temperature features ($\tau = 0.1$, $L_s = 120°$) [from *Forget et al.*, 1998b].

(kg m^{-2} s^{-1}) predicted by the GCM, r is the mean effective radius of the entire layer of CO_2 ice particles, and $\mathcal{T}$ is the characteristic timescale of snow evolution (particle aggregation on the surface). The value r was fixed to 100 μm, as expected from microphysical considerations, and $\mathcal{T}$ was fixed to 0.5 day, in accordance with the typical timescale of the observed low-emission zones [*Kieffer et al.*, 1976; *Forget et al.*, 1995]. Without tuning the model parameters, we have been able to accurately reproduce the general behavior of the low-emission zones observed by Viking in the thermal infrared (Figure 6), including their temporal and spatial scales, their intensity, their latitudinal distribution, and their sensitivity to the dustiness of the atmosphere [*Forget et al.*, 1998b].

Overall, this new parameterization, used in combination with the DTM topography and with allowance for a varying atmospheric dust content, allows the GCM to simulate the CO_2 condensation-sublimation cycle realistically. In particular, the seasonal variations of the surface pressure recorded by the Viking Landers are reproduced without artificially decreasing the condensation rate as was done in previous studies [e.g.. *Hourdin et al.*, 1995; *Pollack et al.*, 1993] by reducing the global emissivity of the caps.

8. Model Performance: Mean State of the Atmosphere

In this section we briefly present the zonal mean circulation simulated at various seasons by the model. We particularly discuss those aspect of the circulation which are relatively new compared to the reference articles from the previous models [*Haberle et al.*, 1993b; *Hourdin et al.*, 1993; *Wilson and Hamilton*, 1996]. For each season, the seasonal variation of the amount of dust in the atmosphere and its distribution is designed to roughly simulate the Viking years without the global dust storms peaks of the first year. The total optical depth at 700 Pa is $\tau = 0.7 + 0.3\cos(L_s + 80°)$ with L_s being the solar longitude [see *Lewis et al.*, this issue, Figure 2]. Although many simulations have been performed with other dust scenarios, they are not described here. The dust properties at solar wavelenghts from *Clancy and Lee* [1991] are used.

8.1. Northern Winter Solstice: a Global Hadley Cell

Figure 7 shows the general aspect of the zonal mean thermal structure and global circulation of the Martian atmosphere just after northern winter solstice. This is a dusty season in the Viking year scenario, and the dust visible optical depth at this time in the simulation is around 1. With such a strong diabatic forcing, the mean performances of the grid point and spectral models have been found to be very similar.

The thermal structure in the lower regions of the summer hemisphere is comparable to the results obtained by other models [*Haberle et al.*, 1993b; *Wilson and Hamilton*, 1996]. The most striking difference from the GCM results obtained in the early 1990s is in the winter polar night, where a strong warming of the atmosphere is simulated between 25 and 80 km above the pole. Such a warming has been observed during northern winter [*Théodore et al.*, 1993; *Santee and Crisp*, 1993]. It was especially strong and its effects penetrated to relatively low altitudes during the second Viking global dust storm, creating the so-called "polar warming event" detected by the IRTM 15-μm channel [*Jakosky and Martin*, 1987]. However, this warming had never been successfully simulated by GCMs until recently, in spite of the numerous studies undertaken [e.g., *Haberle et al.*, 1982, 1993b; *Barnes and Hollingsworth*, 1987; *Zurek and Haberle*, 1988; *Barnes*, 1990; *Hollingsworth*, 1992; *Théodore et al.*, 1993]. This was almost certainly due to the use of an insufficiently deep domain. As first shown by *Wilson* [1997] and *Forget et al.* [1996], raising the model top beyond 90 km altitude allows for the full development of the circulation and can dramatically modify the thermal structure down to altitudes as low as 20 km. In Figure 7b one can see that the warming results from strong meridional winds above 50 km which induce a convergence of mass above the polar region. This convergence forces a descent onto the polar regions and an adiabatic warming at much lower altitude.

Wilson [1997] first correctly described the main mechanism that controls the solsticial zonal-mean circulation and in particular creates the mass convergence in the polar regions [see also *Barnes and Haberle*, 1996]. A complementary version is given here. The streamlines of the mean meridional circulation presented in Figure 7f show that the circulation is dominated by a quasi-global Hadley cell extending from 60°S almost to the north pole. This is an interesting behavior since it has often been argued for the Earth and also for Mars [*Haberle et al.*, 1982; *Zurek et al.*, 1992] that the extension of an inviscid Hadley circulation is limited to the low and mid latitudes because of the conservation of angular momentum (an atmospheric particle leaving the tropics and conserving its angular momentum would acquire a very high zonal velocity in the polar region; its poleward motion would thus be inhibited by the Coriolis and centifugal forces detailed below). This is not true on Mars, where the solsticial Hadley circulation results from a pole to pole heating gradient. In particular, there is no reason for the ascending branch of the Hadley cell to lie directly over the subsolar point as is often assumed [e.g., *Zurek et al.*, 1992]. This branch reaches higher latitudes if the thermal forcing is very strong, for instance, when the atmosphere dustiness in-

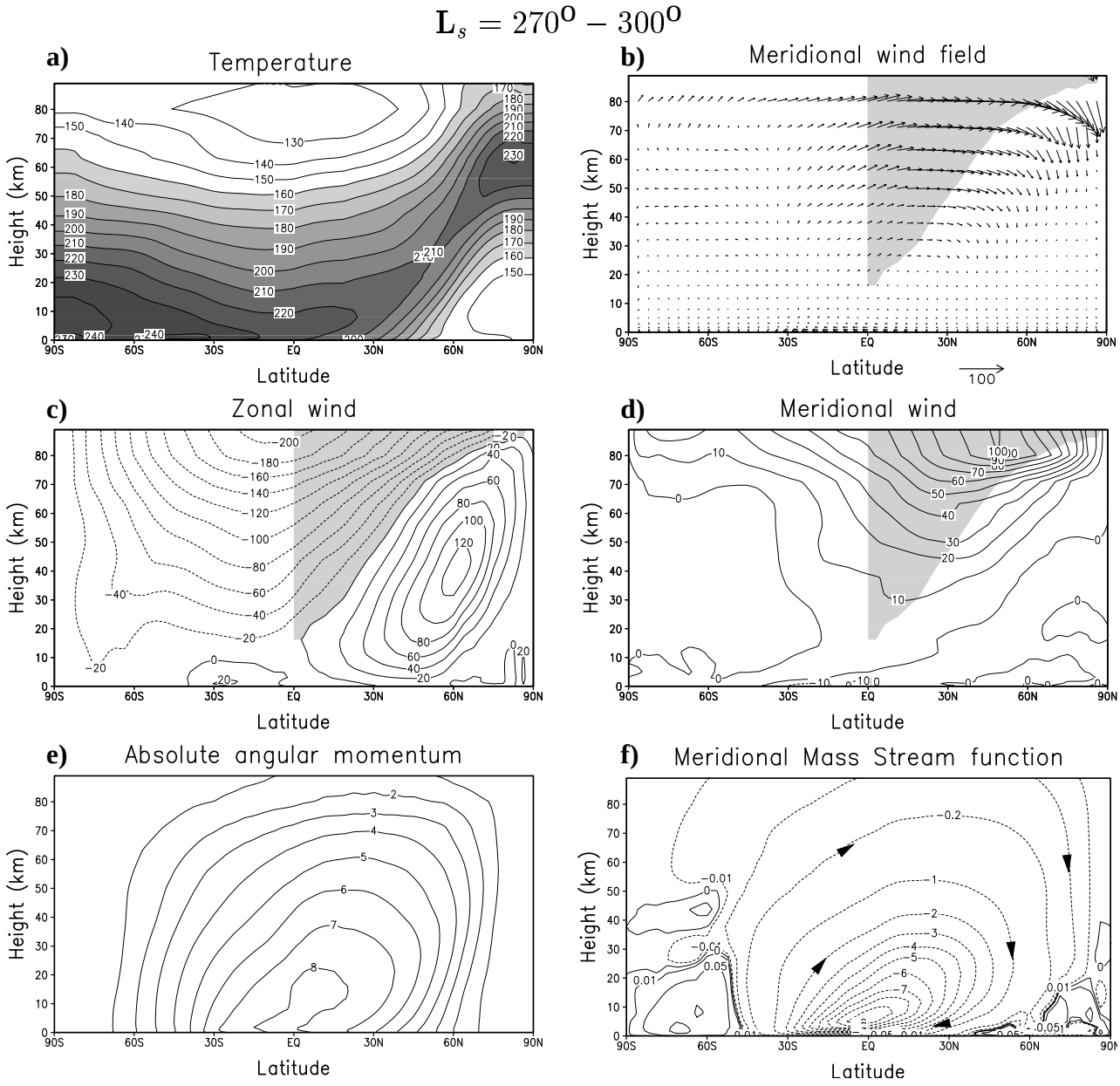

Figure 7. Time-mean section of zonal-mean temperature (K), zonal wind, meridional wind (m s^{-1}), absolute angular momentum (10^8 kg m^2 s^{-1}) and meridional stream function (10^9 kg s^{-1}) during early northern winter ($L_s = 270° - 300°$) as simulated with the grid point model. The spectral model gives almost exactly the same mean results for this season. Shaded areas in Figures 7b-7d show where the Coriolis and centrifugal forces contribute to accelerate the meridional poleward motion instead of slowing it as on Earth. The vertical coordinate is a pseudo-altitude above the ground: $z = H \ln(p/p_0)$, where p/p_0 is the pressure normalized by its local value at the surface and H a fixed scale height $H = 10$ km.

creases. In such conditions an atmospheric particle leaving the high latitudes of the southern hemisphere can cross the equator at high altitude and reach the high northern latitudes while conserving its angular momentum.

On the basis of these considerations one can explain the strength of the mean meridional circulation in the northern hemisphere and thus the polar warming. Consider an atmospheric particle leaving the southern hemisphere from latitude $\phi_0 < 0$ with negligible zonal velocity. On going north, angular momentum conservation at latitude ϕ would result in a negative zonal velocity as long as $|\phi| < |\phi_0|$ (the particle is then farther from the rotation axis than originally) and a positive zonal velocity at higher latitudes ($|\phi| > |\phi_0|$). This behavior is clearly seen throughout most of Figure 7c, indicating that conservation of angular momentum is approximately satisfied throughout a large part of the Martian atmosphere. Such behavior is also apparent in the near coincidence of angular momentum and mass stream function contours in large regions of Figures 7e and 7f. In the rotating frame the zonal velocity u induces an acceleration γ on a fluid particle (owing to Coriolis and centrifugal accelerations) whose northward component is given by

$$\gamma = -u[2\Omega \sin\phi + \frac{u \tan\phi}{a}], \qquad (37)$$

where a and Ω are the planetary radius and rotation rate, respectively. In the northern hemisphere, if $u > 0$, these terms tend to slow, and ultimately stop, the poleward motion of the upper branch of the Hadley circulation. If $u < 0$ in the northern hemisphere, however, γ will tend to accelerate the northward flow (as long as the Coriolis term dominates the centrifugal acceleration, which is true wherever $|u| < |2\Omega a \cos\phi|$). This is the case in a large part of the atmosphere, as indicated by the shaded region in Figures 7b-7d. There, the fluid particles in the upper branch of the Hadley circulation experience a northward acceleration due to γ, in addition to that due to the gradient of diabatic heating, all the way to the pole. As a result, the meridional wind shown in Figure 7d continuously increases in the shaded area in the direction of v between the equator and the $u = 0$ line, where the sign of the zonal wind changes, resulting in considerable mass convergence and thus descending motion over the pole and the observed polar warming.

If angular momentum were to be exactly conserved in the northern hemisphere, $u < 0$ would be found as long as fluid particles in the Hadley cell had not crossed the opposite of the southerly latitude ϕ_0 from which they had started with negligible zonal velocity. At higher latitudes, u would become positive, resulting in a smooth deceleration of the meridional flow toward the pole. However, we find that u can remain negative all the way to the north pole in Figure 7c. This implies some departures from angular momentum conservation in the transport by the meridional circulation, which must be due to the interaction with nonaxisymmetric eddies, leading to marked changes not only in the zonal flow, but also in the meridional circulation itself with a consequent enhancement of the thermal inversion above the pole. This impact of the waves can be roughly estimated by using simplified versions of the model. Simulations carried out by removing the gravity wave drag indicate that the role of these waves is negligible at this season. Simulations performed with the GCM employing diurnally averaged solar radiation (i.e., with no thermal tides) exhibit a quasi-global Hadley cell similar to the full model simulations accompanied by a strong polar warming, but the reduced wave-mean flow interaction decreases the meridional wind by about 30-50 m s^{-1} above 70 km in the northern hemisphere. The corresponding polar warming maximum is slightly shifted away from the pole, and temperatures above the pole are lowered by 20-30 K between 30 and 70 km. Similar results are obtained with a 2-D, axisymmetric version of the model with no planetary waves at all. This suggests that the wave-mean flow interaction discussed here is dominated by thermal tides, as also found by *Wilson* [1997].

As on Earth, the thermal structure of the atmosphere within the Hadley cell is mostly controlled by the dual constraints of angular momentum conservation and thermal wind balance, except in those regions where wave-zonal flow interaction is important. In such conditions the atmospheric temperature can be far from radiative equilibrium over a large part of the planet. This is especially true in the northern hemisphere where the warming occurs, but also in the southern hemisphere during northern winter above 50-60 km where a strong adiabatic cooling may occur. There, the more dust that is in the lower atmosphere, the cooler temperatures become because the Hadley circulation is then more intense. In such conditions the atmospheric gas which is far from radiative equilibrium in the upper branch of the Hadley cell experiences net diabatic radiative heating during its motion, leading to temperatures which are significantly higher in the subsiding branch of the Hadley cell where the polar warming occurs than the ones at the same pressure level in the ascending branch (Figures. 7a and 7f).

8.2. Northern Summer

Figure 8 shows the mean charateristics of the thermal structure and general circulation as simulated by the grid point and spectral models shortly after northern summer solstice. The thermal forcing at this time is weaker than at northern winter solstice because of the smaller amount of dust in the atmosphere (mean opacity around 0.4 in our simulation) and the reduced solar flux near aphelion. Conse-

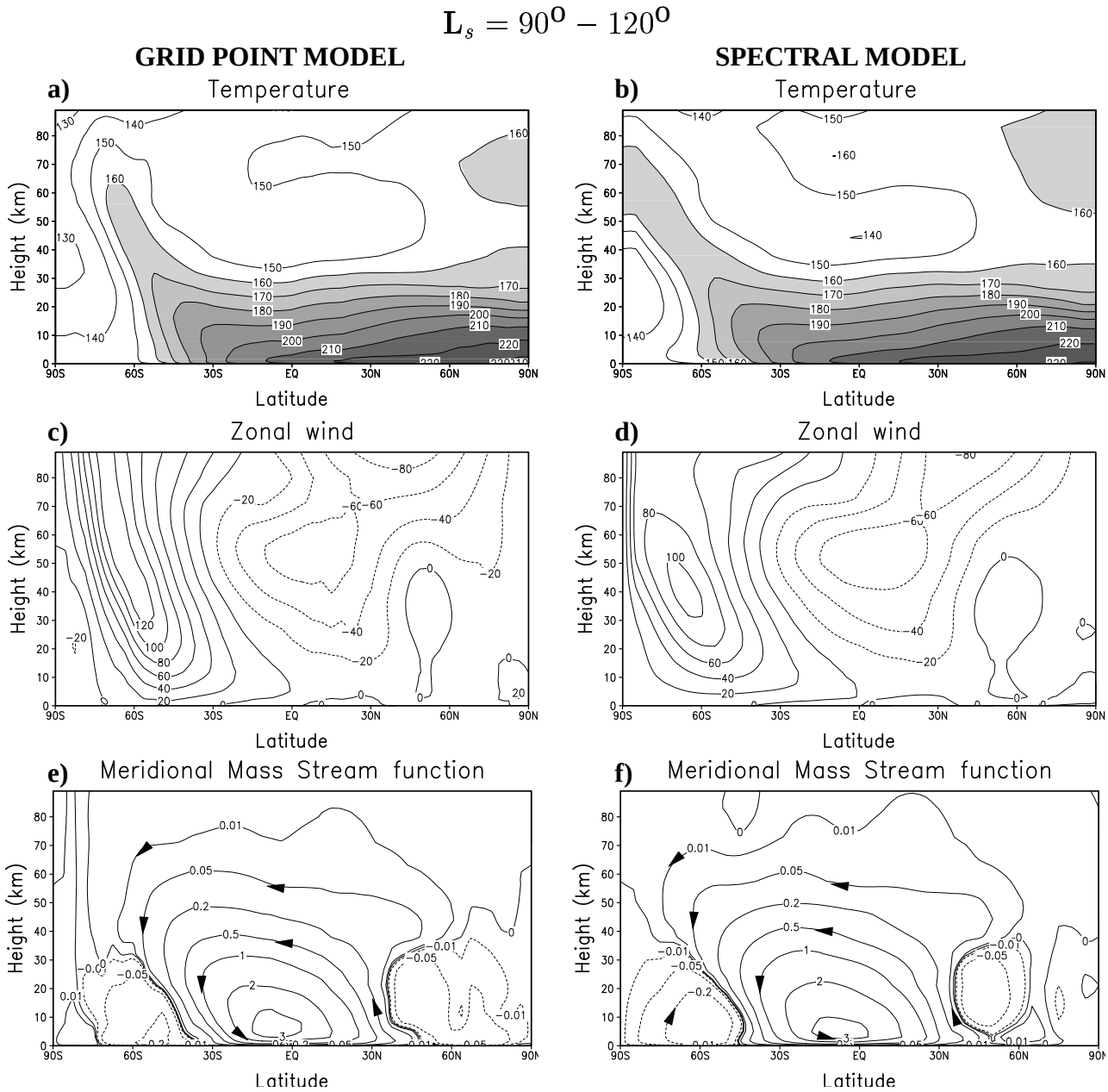

Figure 8. Time-mean section of zonal-mean temperature (K), zonal wind (m s^{-1}) and meridional stream function (10^9 kg s^{-1}) during early northern summer ($L_s = 90° - 120°$) as simulated with the LMD grid point and AOPP spectra models. As in Figure 7, the vertical coordinate is a pseudo-altitude above the ground.

quently, the Hadley circulation is much less intense. Nevertheless, the upper polar atmosphere exhibits a warming at high altitude which results from processes similar to the one described at winter solstice, though much weaker. Such a southern winter polar warming, however, has been observed on Mars [*Deming et al.*, 1986]. In the simulations the temperature inversion extends farther to the pole in the spectral model than in the grid point version, whereas there is a very good agreement between the two models below 50 km. Further analysis shows that the the upper part of the Hadley circulation which creates this warming is not as inviscid as described before and that its extension poleward of 50°S is largely due to wave-mean flow interaction. Planetary, tidal, and gravity waves (see below) tend here to enhance the meridional circulation, mostly by decelerating the westerly jet of the winter hemisphere. It appears that the planetary and tidal wave activity and the related wave-mean flow interaction are stronger in the spectral model, as suggested by the reduced velocity of the zonal wind above 60 km. Sensitivity studies performed with $n = 3$ in the horizontal dissipation operator of both models (see section 3) yielded similar results. This seems to indicate that the difference between the two models does not result from this particular scheme.

Figures 9e and 9f

8.3. Impact of Gravity Wave Drag.

Because the diabatic forcing of the mean circulation is weak at that time, northern summer provides an interesting case to illustrate the impact of the gravity wave parameterization in the GCM. show the zonal mean intensity of the drag (in m s^{-1} per Martian day) in the full model for this season. The gravity wave drag is especially strong in the upper part of the zonal winter jet, where the contrast between the mean flow velocity and the near-zero phase speed of the waves (toward which the speed of the flow is decelerated) is high. This strong drag results from the strong surface winds and from the fact that gravity waves can propagate vertically and break higher up within such a zonal jet. In comparison, the other maximum observed near 20°N between 30 and 40 km (5 m s^{-1} sol^{-1}) is also due to strong surface winds, but the lower zonal wind velocity makes the waves brake lower than in winter jet, and the resulting drag is much smaller. Consequently, the winter jet simulated by the full model is about 10-20 m s^{-1} weaker than when the gravity wave scheme is turned off (compare Figures 8c and 9b). As expected, this additional friction acting on the zonal wind enhances the meridional circulation toward the pole around 50-60 km altitude. This tends to shift the jet poleward (thus increasing the zonal wind near the pole in Figure 9d) and enhances the mass convergence at high latitude. Consequently, the gravity wave drag increases the strength of the polar temperature inversion from 20 km to the top of the model (Figure 9c). Also, the Hadley circulation is globally intensified at high altitude resulting in a stronger retrograde summer jet (Figure 9d) and an adiabatic cooling of the equatorial middle atmosphere (Fig. 9c). It must be noted that the impact of the gravity wave drag is sensitive to the model parameters. For instance, in a similar run performed with *Ockert-Bell et al.*'s [1997] dust properties which yield slightly higher temperatures in the lower atmosphere, the gravity wave drag is almost identical to the case shown in Figures 9e and 9f but it induces a warming of the winter atmosphere above 30 km approximately twice as strong.

8.4. Equinox: A Model-Sensitive Upper Atmosphere

Figures 10 and 11 show the respective mean states of the atmosphere in the model during early northern spring and fall. The low atmosphere is globally in approximate agreement with the results of *Haberle et al.* [1993b]. The general circulation is dominated by two prograde midlatitude jets corresponding to the equator to pole heating gradients at low altitude with a single Hadley cell in each hemisphere. Above 40 km, however, the atmosphere proves to be very sensitive to the kind of dynamical model core. Nevertheless, for both seasons both versions of the model predict a dynamically driven temperature inversion at 60-70 km above both poles.

During northern spring (Figure 10), a strong retrograde jet is simulated above the equator. Interestingly, *Lellouch et al.* [1993] observed such retrograde winds using Doppler-shift measurements of Martian CO microwave spectra. A -120 m s^{-1} equatorial velocity near 60 km was estimated at $L_s = 19°$, which is actually much stronger than the time-mean zonal-mean winds shown in Figure 10. However, the equatorial winds actually simulated at 60 km are highly variable, ranging from 0 to -100 m s^{-1} depending on longitude and time of day. Thus the simulations may not be significantly incompatible with the observations, though more observational data are needed to confirm this. Further investigation of the present simulations showed that the retrograde jet totally disappears in the version of the GCM employing diurnally averaged solar radiation, suggesting that the momentum flux divergence associated with the diurnal tides is a major factor driving the jet. A detailed analysis of these processes is ongoing and will be published in a later paper. The equatorial retrograde jet is stronger in the spectral model, indicating that the thermal tide wave-mean flow interaction is more "efficient" in this version. Similarly, the midlatitude westerly jets are more clearly closed above 60 km by the wave-mean flow interaction in the spectral model, resulting in stronger polar inversions.

During northern fall (Figure 11) the difference between

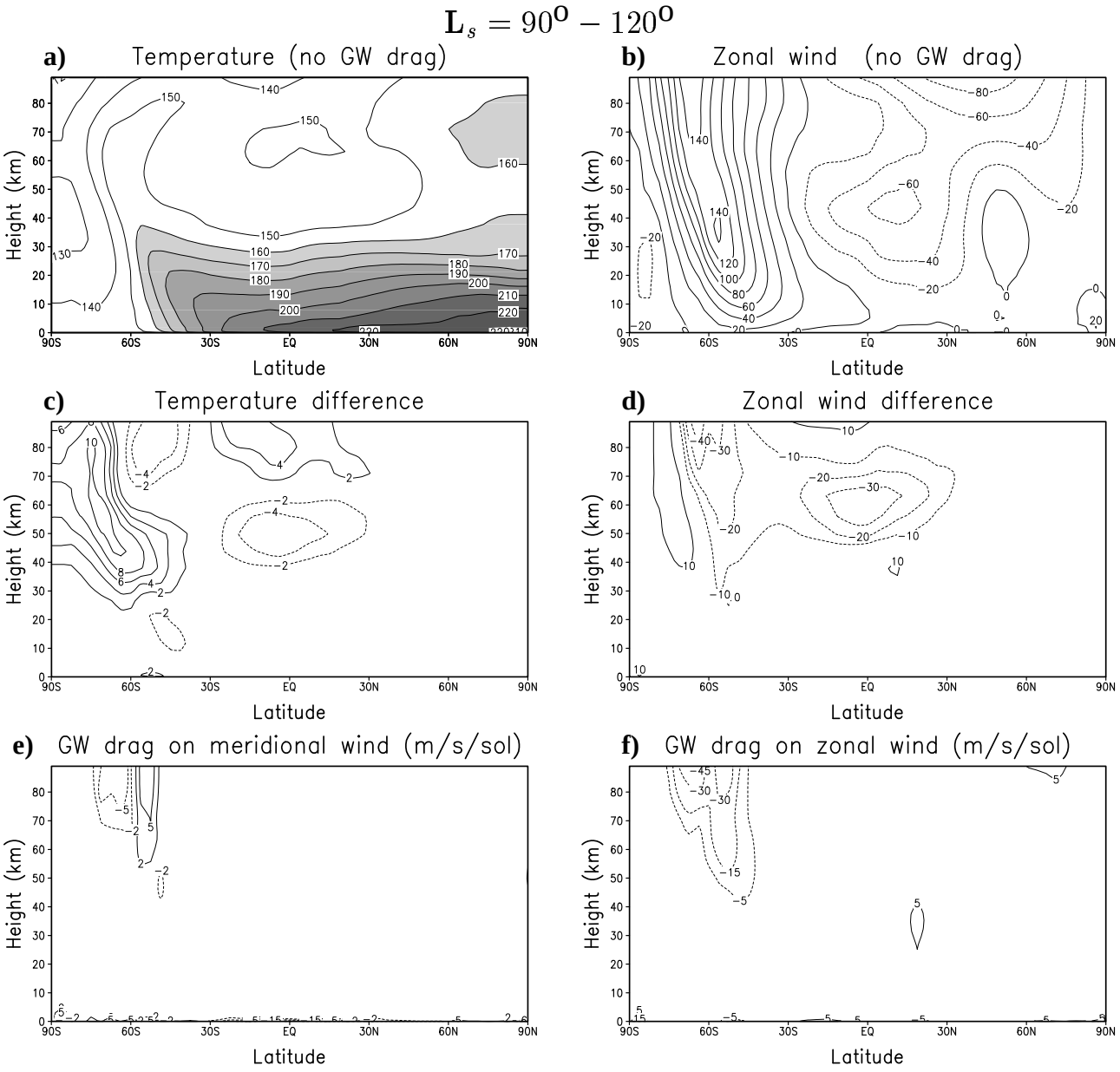

Figure 9. (Figure 9a) Mean zonal wind (m s^{-1}) and (Figure 9b) temperature (K) simulated by the LMD grid point model during early northern summer with the gravity waves scheme turned off. (Figures 9c and 9d) Corresponding difference fields from the full model (Figure 8), illustrating the impact of the gravity waves in this case (Figures 9e and 9f) Mean gravity wave drag on meridional and zonal winds (m s^{-1} sol^{-1}) in the full model. The vertical scale is as in Figure 7.

the tropical middle atmosphere simulated by the two versions of the model is particularly striking. The spectral model shows just a retrograde jet, whereas the grid point model predicts a prograde jet between 60 and 90 km. Such westerlies at the equator (superrotation) require countergradient momentum fluxes [*Hide*, 1969]. Since the prograde jet totally dissapears in the diurnally averaged run, these appear to be also provided by the thermal tides. However, the reason for this important difference has not yet been clearly identified.

9. Conclusion

On the basis of the models we started to create in the early 1990s, we have developed a "new generation" general circulation model of the Martian atmosphere built around two complementary versions of the dynamic core (finite differences or spectral solver). The vertical domain of the model has been extended to above 80 km. This enlarges the field of investigation but also allows the model to better take into account the influence of the upper atmosphere on the lower atmosphere which is found to be far from being negligible on Mars. Conversely, the vertical resolution near the ground has been substantially increased, with a first layer around 5 m above the surface. Within this context, state-of-the-art parameterizations have also been included, together allowing a better simulation of the atmosphere near the surface (boundary layer scheme, subgrid-scale topography parameterization) and at high altitude (gravity wave drag, sponge layer). In addition, the representation of radiative transfer calculations and polar processes representation have been significantly improved.

The mean performance of the model below 40 km is roughly consistent with previous modeling work. One relatively novel aspect, however, is that during the dusty seasons around northern winter solstice, the strong pole to pole diabatic forcing creates a quasi-global, angular-momentum-conserving Hadley cell which extends to the top of the model. In such a cell the Coriolis force, which typically decelerates the mean poleward motion in the terrestrial case, contributes to an acceleration of the poleward meridional wind on Mars. This induces a mass convergence and an adiabatic warming down to 20 km, which had been observed before but had not been properly reproduced in models until recently. In fact, the present studies suggest that thermal inversions can always be expected around 60-70 km above the winter polar regions near solstice and above both poles near equinox. However, our experience with the present model has also shown that the thermal and dynamic structure above 50 km is difficult to predict. First, it must be stated here that the averaged temperatures obtained by the model in this region seem slightly too warm compared to the few observations obtained in situ by spacecrafts [see *Lewis et al.*, this issue] or by Earth-based instruments [*Clancy and Sandor*, 1998]. Also, we have found that very different results can be obtained when using a spectral dynamical core compared to a grid point model. This seems to result from stronger wave-mean flow interactions in the spectral version, but the actual nature of the difference remains unclear. Generally speaking, the Martian upper atmosphere proves to be extremely sensitive to poorly constrained processes, such as gravity wave drag, horizontal dissipation, upper boundary conditions, etc. This high sensitivity is probably due to the strong coupling between the Mars lower and upper atmosphere through vertically propagating waves (tides, gravity, and planetary waves). A large part of this wave activity is able to propagate through the entire modeled atmosphere. Thus, in spite of a very high model top compared to terrestrial GCMs, the representation of the upper boundary conditions (including, e.g., sponge layer to avoid spurious reflection) remains of key importance on Mars. All these uncertainties probably will not be removed by theoretical considerations alone. Observations above 40 km altitude (e.g., from TES and PMIRR limb data) and even above 80 km (e.g., from SPICAM on Mars Express) are needed. Also, the direct measurements of equatorial zonal winds from Doppler shifts in microwave spectral lines, from Earth or, ideally, from a spacecraft, would be extremely useful, since it may not otherwise be possible to determine the circulation in this region from observations.

Acknowledgments.

We thank R. T. Clancy, R. M. Haberle and R. J. Wilson for their comments and suggestions. This work was supported by the European Space Agency through ESTEC TRP contract 11369/95/NL/JG.

References

Anderson, E., and C. Leovy, Mariner 9 television limb observations of dust and ice hazes on Mars, *J. Atmos. Sci.*, *35*, 723–734, 1978.

Baines, P. G., and T. N. Palmer, Rationale for a new physically-based parametrisation of sub-grid scale orographic effects., *Tech. Rep. 169*, Eur. Cent. for Medium-Range Weather Forecasts, Reading, England, 1990.

Barnes, J. R., Possible effect of breaking gravity waves on the circulation of the middle atmosphere of Mars, *J. Geophys. Res.*, *95*, 1401–1421, 1990.

Barnes, J. R., and R. M. Haberle, The Martian zonal-mean circulation: angular momentum and potential vorticity structure in gcm simulations, *J. Atmos. Sci.*, *53*, 3143–3156, 1996.

Barnes, J. R., and J. L. Hollingsworth, Dynamical modeling of a planetary wave mechanism for a Martian polar warming, *Icarus*, *71*, 313–334, 1987.

Barnes, J. R., J. B. Pollack, R. M. Haberle, R. W. Zurek, C. B. Leovy, H. Lee, and J. Schaeffer, Mars atmospheric dynamics

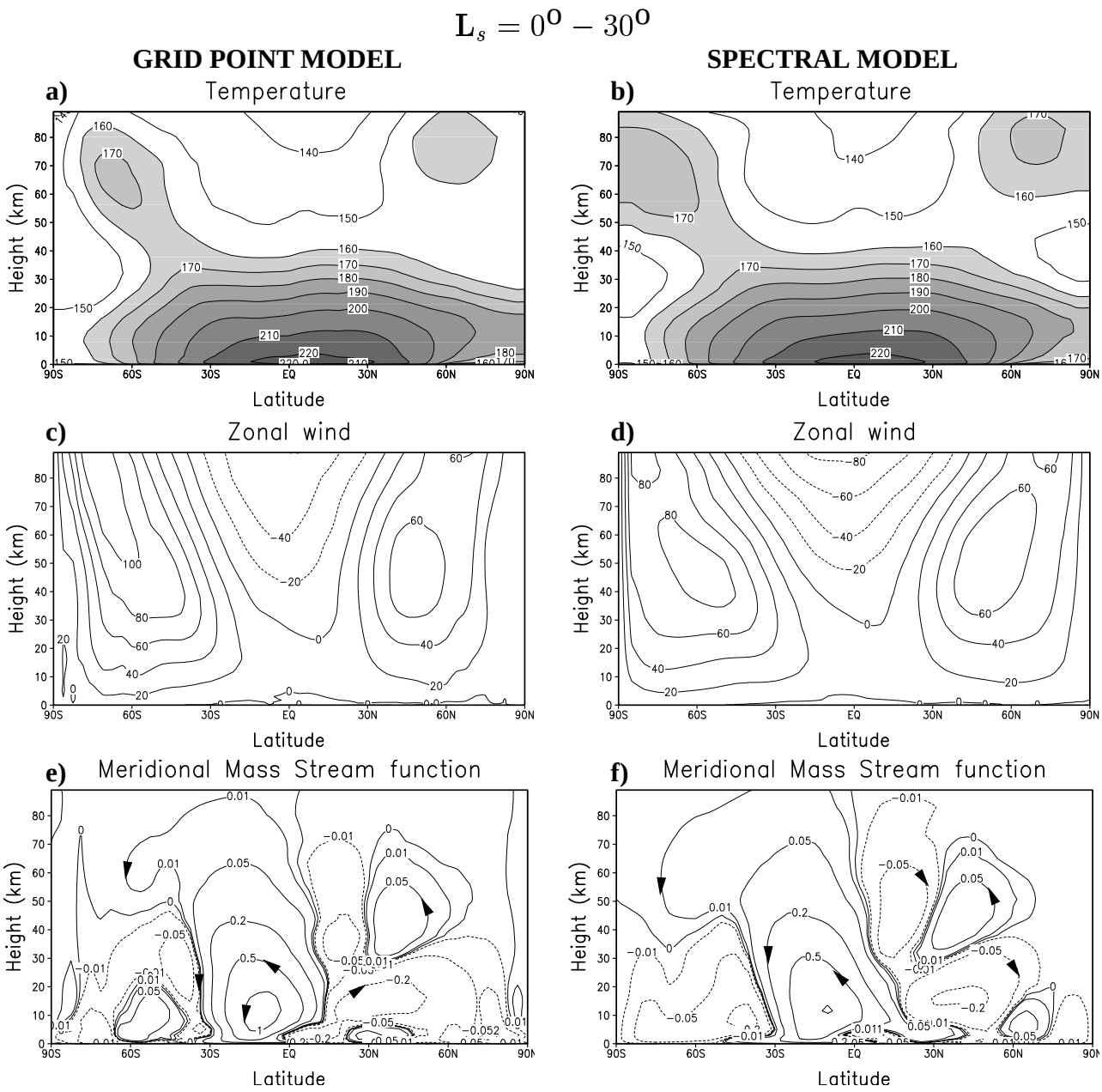

Figure 10. Same as Figure 8 but for early northern spring ($L_s = 0° - 30°$).

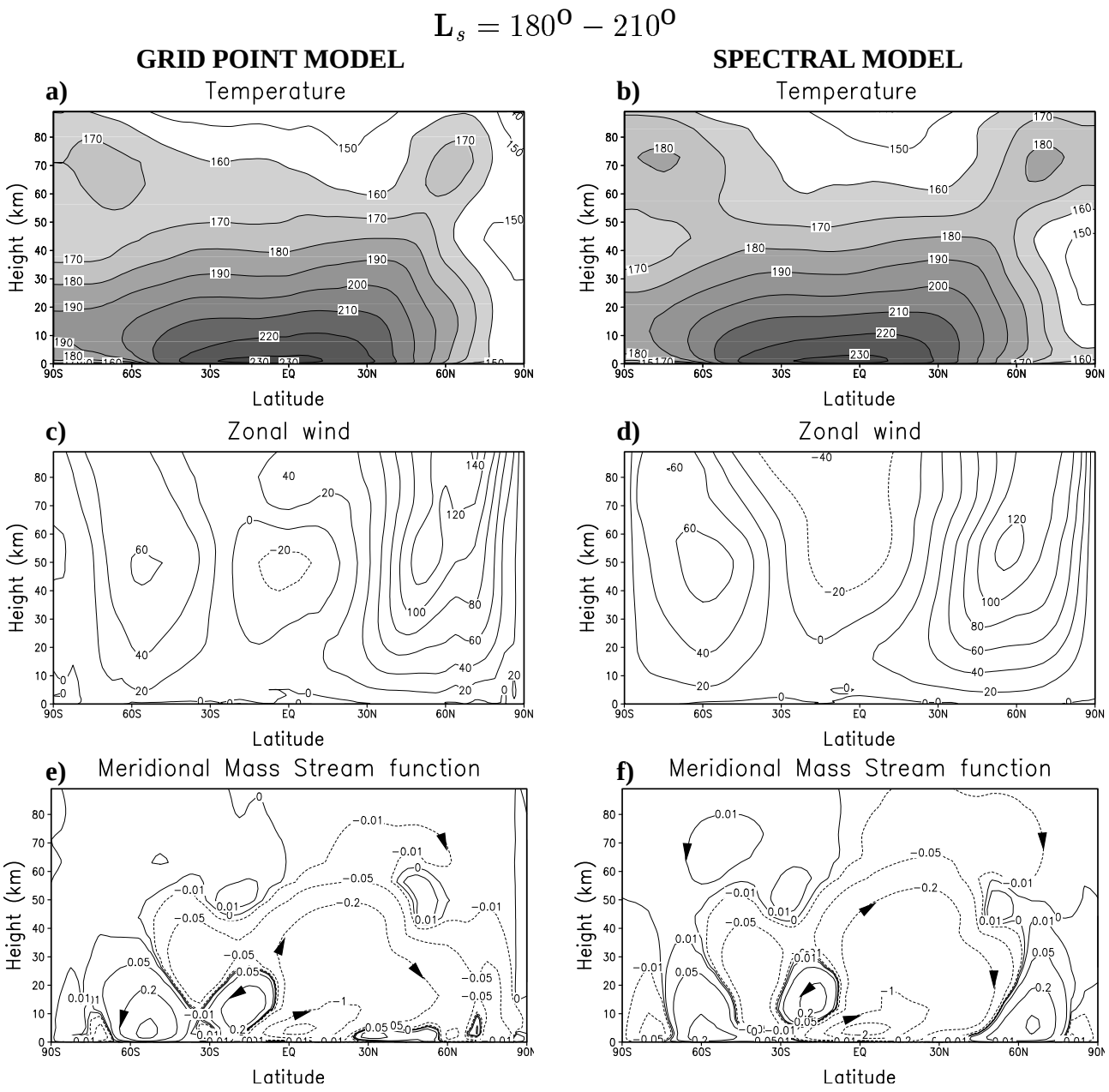

Figure 11. Same as Figure 8 but for early northern fall ($L_s = 180° - 210°$).

as simulated by the NASA/Ames general circulation model, 2, Transient baroclinic eddies, *J. Geophys. Res.*, *98*, 3125–3148, 1993.

Barnes, J. R., R. M. Haberle, J. B. Pollack, H. Lee, and J. Schaeffer, Mars atmospheric dynamics as simulated by the NASA Ames general circulation model, 3, winter quasi-stationary eddies, *J. Geophys. Res.*, *101*, 12,753–12,776, 1996.

Blackadar, A. K., The vertical distribution of wind and turbulent exchange in neutral atmosphere, *J. Geophys. Res.*, *67*, 3095–3102, 1962.

Clancy, R. T., and S. W. Lee, A new look at dust and clouds in the Mars atmosphere: Analysis of emission-phase function sequences from global Viking IRTM observations, *Icarus*, *93*, 135–158, 1991.

Clancy, R. T., and B. J. Sandor, Co_2 ice clouds in the upper atmosphere of Mars, *Geophys. Res. Lett.*, *25*, 489–492, 1998.

Clancy, R. T., S. W. Lee, G. R. Gladstone, W. W. McMillan, and T. Rousch, A new model for Mars atmospheric dust based upon analysis of ultraviolet through infrared observations from Mariner 9, Viking, and Phobos, *J. Geophys. Res.*, *100*, 5251–5263, 1995.

Colburn, D. S., J. B. Pollack, and R. M. Haberle, Diurnal variations in optical depth at Mars, *Icarus*, *79*, 159–189, 1989.

Collins, M., and I. N. James, Regular and irregular baroclinic waves in a simplified global circulation model of the Martian atmosphere, *J. Geophys. Res.*, *100*, 14,421–14,432, 1995.

Collins, M., S. R. Lewis, P. L. Read, and F. Hourdin, Baroclinic wave transitions in the Martian atmosphere, *Icarus*, *120*, 344–357, 1996.

Collins, M., S. Lewis, and P. L. Read, Gravity wave drag in a global circulation model of the Martian atmosphere: parametrisation and validation, *Adv. Space Res.*, *44*, 1395–1409, 1997.

Conrath, B. J., Thermal structure of the Martian atmosphere during the dissipation of dust storm of 1971, *Icarus*, *24*, 36–46, 1975.

Davies, M. E., R. M. Batson, and S. C. W. Sherman, Geodesy and cartography of Mars, in *Mars*, pp. 321–342, Univ. of Ariz. Press, Tucson, 1992.

Deming, D., M. J. Mumma, F. Espenal, T. Kostiuk, and D. Zipoy, Polar warming in the middle atmosphere of Mars, *Icarus*, *66*, 366–379, 1986.

Forget, F., Improved optical properties of the Martian atmospheric dust for radiative transfer calculations in the infrared, *Geophys. Res. Lett.*, *25*, 1105–1109, 1998.

Forget, F., and J. Pollack, Thermal infrared observations of the condensing Martian polar caps: CO_2 ice temperatures and radiative budget, *J. Geophys. Res.*, *101*, 16,865–16,880, 1996.

Forget, F., J. B. Pollack, and G. B. Hansen, Low brightness temperatures of Martian polar caps: CO_2 clouds or low surface emissivity?, *J. Geophys. Res.*, *100*, 21,119–21,234, 1995.

Forget, F., F. Hourdin, and O. Talagrand, Simulation of the Martian atmospheric polar warming with the LMD general circulation model, *Ann. Geophys.*, *14*, C797, 1996.

Forget, F., F. Hourdin, C. Hourdin, and O. Talagrand, Simulation of dust lifting and transport with the LMD Mars general circulation model, *Bull. Am. Astron. Soc.*, *30*, 1023, 1998a.

Forget, F., F. Hourdin, and O. Talagrand, CO_2 snow fall on Mars: Simulation with a general circulation model, *Icarus*, *131*, 302–316, 1998b.

Fouquart, Y., and B. Bonnel, Computations of solar heating of the Earth's atmosphere: A new parametrization, *Contrib. Atmos. Phys.*, *53*, 35–62, 1980.

Galperin, B. A., L. H. Kantha, S. Hassid, and A. Rosati, A quasi-equilibrium turbulent energy model for geophysical flows, *J. Atmos. Sci.*, *45*, 55–62, 1988.

Haberle, R., H. C. Houben, R. Hertenstein, and T. Herdtle, A boundary layer model for Mars: Comparison with Viking Lander and entry data, *J. Atmos. Sci.*, *50*, 1544–1559, 1993a.

Haberle, R. M., and B. M. Jakosky, Atmospheric effects on the remote determination of thermal inertia of Mars, *Icarus*, *90*, 187–204, 1991.

Haberle, R. M., C. B. Leovy, and J. B. Pollack, Some effects of global dust storms on the atmospheric circulation of Mars, *Icarus*, *50*, 322–367, 1982.

Haberle, R. M., J. B. Pollack, J. R. Barnes, R. W. Zurek, C. B. Leovy, J. R. Murphy, H. Lee, and J. Schaeffer, Mars atmospheric dynamics as simulated by the NASA/Ames general circulation model, 1, the zonal-mean circulation, *J. Geophys. Res.*, *98*, 3093–3124, 1993b.

Hide, R., Dynamics of the atmospheres of the major planets with an appendix on the viscous boundary layer at the rigid boundary surface of an electrically conducting rotating fluid in the presence of a magnetic field, *J. Atmos. Sci.*, *26*, 841–853, 1969.

Hollingsworth, J. L., Modeling the forced planetary waves in the Mars atmosphere, Ph.D. thesis, Oreg. State Univ., Corvallis, 1992.

Hollingswoth, J. L., R. M. Haberle, J. Barnes, a. f. c. Bridger, J. B. Pollack, H. Lee, and J. Schaeffer, Orographic control of storm zones on mars, *Nature*, *380*, 413–416, 1996.

Hoskins, B. J., and A. J. Simmons, A multi-layer spectral model and the semi-implicit method, *Q. J. R. Meteorol. Soc.*, *109*, 771–783, 1975.

Hourdin, F., A new representation of the CO_2 15 μm band for a Martian general circulation model, *J. Geophys. Res.*, *97*, 18,319–18,335, 1992a.

Hourdin, F., Conservation du moment angulaire dans le modèle de circulation générale du LMD, *Note Interne 175*, Lab. de Météorol Dyn., Cent. Nat. de la Rech. Sci., Paris, 1992b.

Hourdin, F., P. Le Van, F. Forget, and O. Talagrand, Meteorological variability and the annual surface pressure cycle on Mars, *J. Atmos. Sci.*, *50*, 3625–3640, 1993.

Hourdin, F., F. Forget, and O. Talagrand, The sensitivity of the Martian surface pressure to various parameters: A comparison between numerical simulations and Viking observations, *J. Geophys. Res.*, *100*, 5501–5523, 1995.

Jakosky, B. M., and T. Z. Martin, Mars: North-polar atmospheric warming during dust storms, *Icarus*, *72*, 528–534, 1987.

Jaquin, F., P. Gierasch, and R. Kahn, The vertical structure of limb hazes in the Martian atmosphere, *Icarus*, *68*, 442–461, 1986.

Joshi, M. M., S. R. Lewis, P. L. Read, and D. C. Catling, Western boundary currents in the atmosphere of Mars, *Nature*, *367*, 548–551, 1994.

Kieffer, H. H., S. C. Chase, E. D. Miner, F. D. Palluconi, G. Münch, G. Neugebauer, and T. Z. Martin, Infrared thermal mapping of the Martian surface and atmosphere: First results, *Science*, *193*, 780–786, 1976.

Lellouch, E., J. J. Goldstein, S. Bougher, B. Theodore, and J. Rosenqvist, Mars' middle atmosphere circulation near equinox from microwave observations, *Bull. Am. Astron. Soc.*, *25*, 1060, 1993.

Leovy, C., and Y. Mintz, Numerical simulation of the atmospheric circulation and climate of Mars, *J. Atmos. Sci.*, *26*, 1167–1190, 1969.

Lewis, S. R., P. L. Read, and M. Collins, Martian atmospheric data assimilation with a simplified general circulation model: orbiter and lander networks, *Planet. Space Sci.*, *44*, 1395–1409, 1996.

Lewis, S. R., M. Collins, P. L. Read, F. Forget, F. Hourdin, R. Fournier, C. Hourdin, O. Talagrand, and J.-P. Huot., A climate database for Mars, 1999, *J. Geophys. Res.*, this issue.

Lindner, B. L., The Martian polar cap: Radiative effects of ozone, clouds, and airborne dust, *J. Geophys. Res.*, *95*, 1367–1379, 1990.

Lindzen, R. S., Turbulence and stress owing to gravity wave and tidal breakdown, *J. Geophys. Res.*, *86*, 9707–9714, 1981.

Lopez-Puertas, M., and M. Lopez-Valverde, Radiative energy balance of CO_2 non-LTE infrared emissions in the Martian atmosphere, *Icarus*, *114*, 113–129, 1995.

Lott, F., and M. Miller, A new sub-grid scale orographic drag parametrization: its formulation and testing., *Q. J. R. Meteorol. Soc.*, *123*, 101–128, 1997.

MacVean, M. K., The effect of horizontal diffusion on baroclinic development in a spectral model, *Q. J. R. Meteorol. Soc.*, *38*, 771–783, 1983.

Markiewicz, W. J., R. M. Sablotny, H. U. Keller, N. Thomas, D. Titov, and P. H. Smith, Optical properties of the Martian aerosols as derived from imager for Mars Pathfinder midday sky brightness data, *J. Geophys. Res.*, *104*, 9009–9017, 1999.

Martin, T. Z., Thermal infrared opacity of the Mars atmosphere, *Icarus*, *66*, 2–21, 1986.

Martin, T. Z., and M. I. Richardson, New dust opacity mapping from Viking infrared thermal mapper data, *J. Geophys. Res.*, *98*, 10,941–10,949, 1993.

Mellor, G. L., and T. Yamada, Development of a turbulence closure model for geophysical fluid problems, *Rev. of Geophys.*, *20*, 851–875, 1982.

Miller, M. J., P. M. Palmer, and R. Swinbank, Parametrisation and influence of sub-grid scale orography in general circulation and numerical weather prediction models., *Meteorol. Atmos. Phys.*, *40*, 84–109, 1989.

Morcrette, J. J., L. Smith, and Y. Fouquart, Pressure and temperature dependence of the absorption in longwave radiation parametrizations, *Contrib. Atmos. Phys.*, *59*, 455–469, 1986.

Murphy, J., J. B. Pollack, R. M. Haberle, C. B. Leovy, O. B. Toon, and J. Schaeffer, Three-dimensional numerical simulation of Martian global dust storms, *J. Geophys. Res.*, *100*, 26,357–26,376, 1995.

Ockert-Bell, M. E., J. F. Bell III, C. McKay, J. Pollack, and F. Forget, Absorption and scattering properties of the Martian dust in the solar wavelengths, *J. Geophys. Res.*, *102*, 9039–9050, 1997.

Paige, D. A., and K. D. Keegan, Thermal and albedo mapping of the polar regions of Mars, 2, South polar region, *J. Geophys. Res.*, *99*, 25,993–26,013, 1994.

Paige, D. A., J. E. Bachman, and K. D. Keegan, Thermal and albedo mapping of the polar regions of Mars using Viking thermal mapper observations, 1, North polar region, *J. Geophys. Res.*, *99*, 25,959–25,991, 1994.

Palluconi, F. D., and H. H. Kieffer, Thermal inertia mapping of Mars from 60^{o}S to 60^{o}N, *Icarus*, *45*, 415–426, 1981.

Palmer, T. N., G. J. Shutts, and R. Swinbank, Alleviation of a systematic westerly bias in general circulation and numerical weather prediction models through an orographic gravity wave drag parametrisation, *Q. J. R. Meteorol. Soc.*, *112*, 1001–1039, 1986.

Phillips, S. P., Analytical surface pressure and drag for linear hydrostatic flow over three-dimensional elliptical mountains, *J. Atmos. Sci.*, *41*, 1073–1084, 1984.

Pleskot, L. K., and E. D. Miner, Time variability of Martian bolometric albedo, *Icarus*, *50*, 259–287, 1982.

Pollack, J. B., D. S. Colburn, F. M. Flasar, R. Kahn, C. E. Carlston, and D. Pidek, Properties and effects of dust particles suspended in the Martian atmosphere, *J. Geophys. Res.*, *84*, 2929–2945, 1979.

Pollack, J. B., C. B. Leovy, P. W. Greiman, and Y. Mintz, A Martian General Circulation Model experiment with large topography, *J. Atmos. Sci.*, *38*, 3–29, 1981.

Pollack, J. B., R. M. Haberle, J. Schaeffer, and H. Lee, Simulations of the general circulation of the Martian atmosphere, 1, Polar processes, *J. Geophys. Res.*, *95*, 1447–1473, 1990.

Pollack, J. B., R. M. Haberle, J. R. Murphy, J. Shaeffer, and H. Lee, Simulation of the general circulation of the Martian atmosphere 2, Seasonnal pressure variations, *J. Geophys. Res.*, *98*, 3149–3181, 1993.

Pollack, J. B., M. E. Ockert-Bell, and M. K. Shepard, Viking Lander image analysis of Martian atmospheric dust, *J. Geophys. Res.*, *100*, 5235–5250, 1995.

Sadourny, R., The dynamics of finite-difference models of the shallow-water equations, *J. Atmos. Sci.*, *32*, 680–689, 1975.

Sadourny, R., and K. Laval, January and July performance of the LMD general circulation model, in *New perspectives in Climate Modeling*, edited by A. Berger and C. Nicolis, Elsevier, pp. 173–197, Amsterdam, 1984.

Santee, M., and D. Crisp, Thermal structure and dust loading of the Martian atmosphere during late southern summer: Mariner 9 revisited, *J. Geophys. Res.*, *98*, 3261–3279, 1993.

Savijärvi, H., Radiative fluxes on a dust free Mars, *Contrib. Atmos. Phys.*, *2*, 103–112, 1991.

Smith, D. E., and M. T. Zuber, The shape of Mars and the topographic signature of the hemispheric dichotomy, *Science*, *271*, 184–188, 1996.

Sutton, J. L., C. B. Leovy, and J. E. Tillman, Diurnal variations of the Martian surface layer meteorological parameters during the first 45 sols at two Viking lander sites, *J. Atmos. Sci.*, *35*, 2346–2355, 1978.

Théodore, B., E. Lellouch, E. Chassefiere, and A. Hauchecorne, Solsticial temperature inversions in the Martian middle atmosphere : observational clues and 2-D modeling, *Icarus*, *105*, 512–528, 1993.

Toon, O. B., J. B. Pollack, and C. Sagan, Physical properties of the particles composing the Martian dust storm of 1971-1972, *Icarus*, *30*, 663–696, 1977.

Toon, O. B., C. P. McKay, T. P. Ackerman, and K. Santhanam, Rapid calculation of radiative heating rates and photodissociation rates in inhomogeneous multiple scattering atmospheres, *J. Geophys. Res.*, *94*, 16,287–16,301, 1989.

Wilson, R. J., A general circulation model of the Martian polar warming, *Geophys. Res. Lett.*, *24*, 123–126, 1997.

Wilson, R. W., and K. Hamilton, Comprehensive model simulation of thermal tides in the Martian atmosphere, *J. Atmos. Sci.*, *53*, 1290–1326, 1996.

Wu, S. S. C., Mars synthetic topographic mapping, *Icarus*, *33*, 417–440, 1978.

Zurek, R. W., Martian great dust storm, an update, *Icarus*, *50*, 288–310, 1982.

Zurek, R. W., and R. M. Haberle, Zonally symmetric response to atmospheric tidal forcing in the dusty Martian atmosphere, *J. Atmos. Sci.*, *45*, 2469–2485, 1988.

Zurek, R. W., J. R. Barnes, R. M. Haberle, J. B. Pollack, J. E. Tillman, and C. B. Leovy, Dynamics of the atmosphere of Mars, in *Mars*, pp. 835–933, Univ. of Ariz. Press, Tucson, 1992.

M. Collins, Hadley Centre for Climate Prediction and Research, U.K. Meteorological Office, London Road, Bracknell RG12 2SZ, England. (matcollins@meto.gov.uk)

F. Forget, C. Hourdin, F. Hourdin and O. Talagrand, Laboratoire de Météorologie Dynamique du Centre National de la Recherche Scientifique, Université Paris 6, 4 place Jussieu, 75252 Paris Cedex 05, France. (forget@lmd.jussieu.fr; chourdin@lmd.jussieu.fr; hourdin@lmd.jussieu.fr; talagran@lmd.ens.fr)

R. Fournier, Laboratoire d'Energie Solaire et Thermique de l'Habitat, Université Paul Sabatier, Toulouse, France. (rfo@sphinx.ups-tlse.fr)

J.-P. Huot, Space Systems Environment and Effects Analysis Section, European Space Research and Technology Centre, European Space Agency, Keplerlaan 1, 2200 AG Noordwijk, Netherlands. (jhuot@estec.esa.nl)

S. R. Lewis and P. L. Read, Atmospheric, Oceanic and Planetary Physics, Clarendon Laboratory, Parks Road, Oxford OX1 3PU, England. (s.lewis1@physics.oxford.ac.uk; p.read1@physics.oxford.ac.uk)

January 22, 1999; revised May 11, 1999; accepted May 18, 1999.

This preprint was prepared with AGU's LaTeX macros v4, with the extension package 'AGU++' by P. W. Daly, version 1.5g from 1998/09/14.